Lithos 119 (2010) 621–641

Contents lists available at ScienceDirect

Lithos

journal homepage: www.elsevier.com/locate/lithos

Petrogenesis and tectonic significance of a Mesozoic granite–syenite–gabbro association from inland South China

Zhen-Yu He [a], Xi-Sheng Xu [a,*], Yaoling Niu [b]

[a] State Key Laboratory for Mineral Deposits Research, Department of Earth Sciences, Nanjing University, Nanjing, 210093, China
[b] Department of Earth Sciences, Durham University, Durham DH1 3LE, UK

ARTICLE INFO

Article history:
Received 17 April 2010
Accepted 11 August 2010
Available online 18 August 2010

Keywords:
Asthenosphere upwelling
Early Yanshanian
Far-field stress
Granite–syenite–gabbro
South China

ABSTRACT

A granite–syenite–gabbro association from inland South China has been studied for zircon U–Pb ages and Hf isotopic compositions as well as whole-rock elemental and Sr–Nd isotopic compositions to constrain their sources and tectonic settings. These rocks have distinctive crystallization ages: the Longyuanba biotite granites have a mean age of ~240 Ma, the Longyuanba two-mica granites, Pitou alkali-feldspar granites and amphibole-bearing alkali-feldspar granites, Tabei and Huangbu syenites and Chebu and Chenglong gabbros have a similar age of ~178 Ma, whereas the Dafengnao syenite gives a mean age of ~165 Ma.

The Longyuanba biotite granites and two-mica granites exhibit S-type characteristics, probably derived from a Neoproterozoic crustal source. The Chenglong gabbro has OIB-like trace element and highly depleted isotope compositions ($\varepsilon_{Hf}(t) = 10.0 \pm 1.3$; $\varepsilon_{Nd}(t) = 5.2$), suggesting its parental melt to be of asthenospheric origin with insignificant crustal assimilation. However, crustal contamination is required to explain the isotopic compositions of the Chebu gabbro. The syenites are shoshonitic in composition, and have depleted Sr–Nd–Hf isotopic signatures, which we interpret to have resulted from a mixed source of asthenospheric mantle and metasomatized lithospheric mantle. As expected, the signals of crustal assimilation are conspicuous in the petrogenesis of the more evolved syenites. The Pitou alkali-feldspar granite and amphibole-bearing alkali-feldspar granite exhibit I-type and A-type characteristics, respectively. They are isotopically more depleted than the S-type Longyuanba granites. We suggest that they may have formed through magma mixing of predominantly mantle-derived melts with the Neoproterozoic crust.

The Jurassic granite–syenite–gabbro association was the product of asthenosphere–lithosphere–crust interactions, which records the primary role of asthenospheric mantle upwelling in magma generation both in the mantle and in the crust in the Early Yanshanian time in South China. They probably occurred in an intraplate rift-like environment as a tectonic response to far-field stress at plate margins during the early stage of the paleo-Pacific plate subduction. The tectonic transition from the Tethys orogenic regime to the paleo-Pacific regime was accomplished in the Early Jurassic, and the early Yanshanian magmatism should be genetically associated with the paleo-Pacific tectonic regime.

1. Introduction

Mesozoic granitoids are widespread in South China. They have attracted the interests of many over the last decades because of economically significant mineralization associated with them and because they carry the information on ways in which they were emplaced in response to the tectonic evolution of the region (e.g., Jahn, 1974; Chen and Jahn, 1998; Zhou and Li, 2000; Li and Li, 2007; Wang et al., 2007a,b; Hsieh et al., 2008; Pirajno et al., 2009). These granitoids crop out over a large area of ~135,300 km^2, and were conventionally thought to represent products in response to three orogenic events in time and space, i.e. the Indosinian (Triassic), the Early Yanshanian (Jurassic) and the Late Yanshanian (Cretaceous) (Zhou and Li, 2000; Li et al., 2007). The Indosinian granitoids occur as batholiths distributed discretely in the interior of South China (Fig. 1a). These rocks are mainly coarse- to medium-grained peraluminous granites, and were traditionally regarded as S-type granites (Zhou et al., 2006; Wang et al., 2007b). In contrast, the Early Yanshanian granitoids are dominated by calc-alkaline I-type granites with subordinate A- and S-type granites. They are distributed in the hinterland discretely in the NE–SW direction with the exception in the Nanling region where they define an E–W trend. Volumetrically less abundant early Yanshanian syenites, gabbros and basalts have been found to be associated with the E–W trending granites in the Nanling region (Fig. 1a; Li et al., 2003; 2007; Xie et al., 2006). These latter mafic rocks have attracted much attention because of their mantle origin, providing the opportunity to constrain the source characteristics of the Mesozoic asthenospheric mantle beneath the

* Corresponding author. Tel.: +86 25 83592185; fax: +86 25 83686016.
E-mail address: xsxu@nju.edu.cn (X.-S. Xu).

0024-4937/$ – see front matter © 2010 Elsevier B.V. All rights reserved.
doi:10.1016/j.lithos.2010.08.016

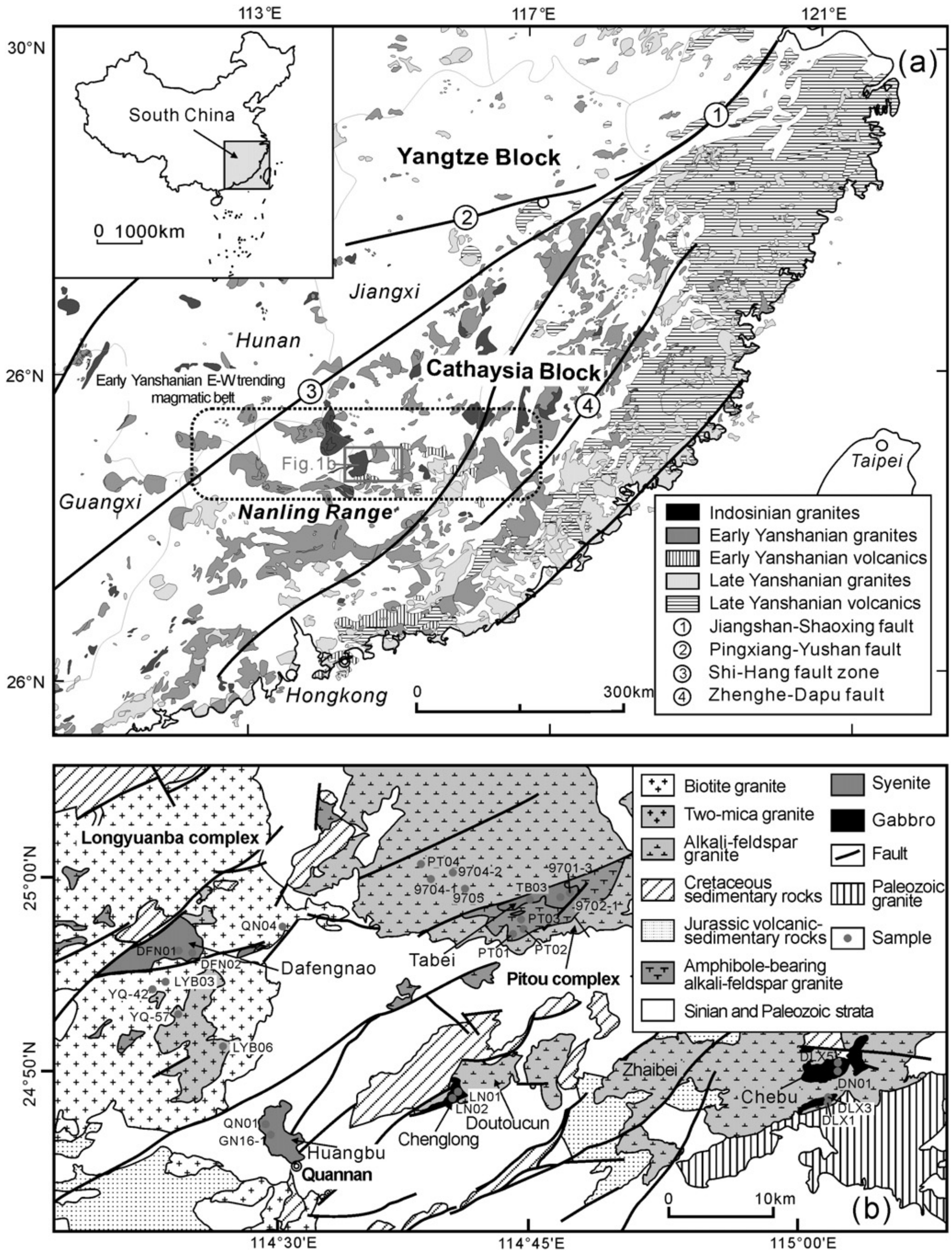

Fig. 1. (a) Simplified geological map of South China showing the distribution of Mesozoic granite-volcanic rocks (modified from Zhou et al., 2006). (b) Geological map of Southern Jiangxi, also showing the locations of samples studied (modified after He et al., 2007).

South China Block (Wang et al., 2003, 2005b, 2008b; Zhou et al., 2005; He et al., 2007; Yu et al., 2010). The Late Yanshanian granitic rocks occur mainly along the coastal region accompanied by vast silicic volcanic rocks, forming a large NE–SW trending magmatic belt (Zhou et al., 2006; Chen et al., 2008a). All these Mesozoic granitoid rocks manifest a first-order temporal trend, progressively younger towards the coastal region in Southeast China.

It is noteworthy that composite granitoid complexes are quite common in South China, apparently formed by multi-stage magma emplacement. Although there is a general consensus that the petrogenesis of these granitoids involves significant crust material (Jahn et al., 1990; Chen and Jahn, 1998), it remains unclear whether they were formed by repeated remelting of the similar crustal materials or resulted from melting of different source rocks. This is a fundamentally important problem because granites contain such information, whose knowledge is key to understanding the role of mantle geodynamics in the petrogenesis of these rocks, thereby understanding the tectonic settings and regional tectonic evolution as well as providing information for models of continental crust accretion (e.g., Mo et al., 2008; Niu and O'Hara, 2009). However, there have been only a few studies of this nature so far. On the other hand, many of the Mesozoic granitoids in South China are highly evolved, and significant compositional similarity exists among granitoid suites of temporally different events (e.g., Li et al., 2007). Furthermore, the lack of effective measure of relative contributions of crust vs. mantle in magma generation makes the petrogenetic studies inconclusive. For example, the well studied Fogang granites in South China have been previously interpreted as S-, I- and A-types by different researchers (Li et al., 2007 and references therein).

There has also been a continued debate on the nature of tectonic settings in which these granitoids were emplaced. In the Mesozoic, there were successive subduction/collision events around the South

China block. At the southwestern margin, the oblique collision along Song Ma suture between the Indochina and South China blocks took place during the Indosinian Orogeny (considered as belonging to the Tethys orogenic regime) in the Early Triassic (Carter et al., 2001; Lepvrier et al., 2004). This collision caused the development of nearly E–W trending compressional deformations in the northern part of the South China block (Zhang et al., 2009) and NW–WNW- and SE–ESE-dipping faults and shear zones in the southern part of the South China Block (Wang et al., 2005c, 2007a), as well as the amalgamation of the Yangtze (South China) and Sino-Korean (North China) blocks along the Qinling-Dabie Orogeny (Meng and Zhang, 2000). To the east was the northwestward subduction of the paleo-Pacific plate beneath the South China block, probably beginning in the Early Jurassic (Jahn, 1974), as manifested by the widespread (though volumetrically less abundant on map view) Early Yanshanian granitoids along the coastal region superimposed by the more abundant Cretaceous granitoids and volcanic rocks (Fig. 1a; also see Jahn, 1974; Zhou et al., 2006; Chen et al., 2007; He et al., 2009). However, the exact timing and geological effects of the Mesozoic tectonic transition from the Tethys orogenic regime to the paleo-Pacific regime remain poorly constrained. The major focus of the debate is whether the Early Yanshanian intraplate continental magmatism in inland South China was genetically associated with the Tethys orogenic regime, or with the paleo-Pacific plate subduction. Several tectonic models have been proposed, including (1) flat-slab subduction of the paleo-Pacific plate during ~250–190 Ma followed by break-off and foundering of the same flat subducting plate in the Early Jurassic to account for both the Indosinian magmatism and the Early Yanshanian intraplate magmatism (Li and Li, 2007; Li et al., 2007); (2) extension-induced post-orogenic magmatism following the Indosinian orogeny (Chen et al., 2002; Wang et al., 2003; Chen et al., 2008b), and (3) far-field response to the early stage subduction of the paleo-Pacific plate at the eastern margin (Zhou et al., 2006).

In order to resolve these debates, we choose to study magmatic rocks in southern Jiangxi province. This is geologically an ideal test ground because of the spatial coexistence of granites that are well constrained to be genetically associated with the Indosinian orogenesis and a granite–syenite–gabbro rock association that is known to be temporally and tectonically associated with Early Yanshanian magmatism. In this paper, we present the results of a detailed geochemical study of these rocks, including zircon U–Pb age dating, zircon Hf isotopic analysis, and whole-rock geochemical analysis. These data offer new perspectives on the petrogenesis of these rocks and the Mesozoic tectonic evolution of Southeast China and contribute to the understanding of granitoid magmatism in general.

2. Geologic background and samples

The South China block has a complex tectonic history, and comprises two major Precambrian continental blocks: the Yangtze block in the northwest, and the Cathysia block in the southeast, divided by the Jiangshan–Shaoxing and Pingxiang–Yushan sutures (Fig. 1a, Chen and Jahn, 1998; Wang et al., 2003; Zhang and Wang, 2007). The Mesozoic magmatism was mainly concentrated in the Cathysia block (Zhou et al., 2006). The Cathysia block can be further divided into the interior (western Cathysia) and coastal (eastern Cathysia) parts along the Zhenghe–Dapu fault (see Chen and Jahn, 1998). Recently, Xu et al. (2007) proposed that the eastern and western Cathysia blocks may have different crustal evolution histories. The former has a basement of dominantly Paleoproterozoic age (1850–2400 Ma) whereas the western Cathysia block is dominated by crust of Neoproterozoic age with minor Archean to Mesoproterozoic components.

The study area is located in the western Cathysia block, where magmatic rocks are abundant and mostly emplaced in the time frame of the Indosinian and Early Yanshanian periods. The Early Yanshanian granites, syenites and gabbros may be regarded as constituents of the Jurassic E–W magmatic belt (Fig. 1a) or previously known as E–W volcanic belt (Chen et al., 2002; Xie et al., 2006; Chen et al., 2008b). The Longyuanba complex, situated ~10 km northwest of the Quannan County, has an outcrop area of ~450 km^2. The complex is made up of biotite granite, two-mica granite and syenite (Fig. 1b). Field mapping shows two main stages of emplacement: an early stage intrusion of biotite granite, and a late-stage intrusion of two-mica granite and Dafengnao syenite. The Pitou complex is intimately juxtaposed to the Longyuanba complex with an exposure area of >400 km^2. It includes alkali-feldspar granite, amphibole-bearing alkali-feldspar granite and syenite. These lithologies show gradational relationships as manifested by spatial variation in mineral modal abundances. Both the Longyuanba and Pitou complexes intruded the Sinian and Paleozoic pelitic and sandy sedimentary rocks without obvious contact metamorphism.

The Huangbu syenite is ~3 km southeast from the Longyuanba complex with an exposure area of ~6 km^2, which was emplaced in the Lower Carboniferous strata (Fig. 1b). The Chebu gabbro is ~15 km southeast of the Pitou complex, and crops out as a few small intrusions with a total outcrop area of ~20 km^2. They are emplaced within the Zhaibei granite with irregular shapes. The Chebu body is predominantly coarse- to medium-grained gabbro, with minor more evolved pyroxene diorite. The Chenglong gabbro is located ~10 km south of the Pitou complex, occupies an area of ~5 km^2, intruded the Cambrian strata, and is in turn intruded by Doutoucun granite along its northern margin (Fig. 1b). For convenience, we call these igneous rocks altogether as a granite–syenite–gabbro association (GSGA) in the subsequent discussion. The lithologies and mineral assemblages of these intrusive complexes/bodies are summarized in Table 1, which also gives GPS positions of samples used in this study.

Samples were analyzed in different laboratories for mineral major elements and back scattered electron (BSE) images, zircon U–Pb

Table 1
Lithologies and mineral assemblages of the GSGA in South Jiangxi.

Complex/body	Lithology	Main minerals	Sample location (GPS position)
Longyuanba complex	Biotite granite	Or + Qtz + Pl + Bt	LYB03 (N24°53′46″ E114°23′46″)
			QN04 (N24°56′59″ E114°30′39″)
	Two-mica granite	Pl + Qtz + Or + Ms + Bt	LYB06 (N24°52′21″ E114°28′28″)
	Syenite	Prt + Qtz + Mag	DFN01 (N24°55′28″ E114°25′46″)
			DFN02 (N24°55′21″ E114°26′18″)
Pitou complex	Alkali-feldspar granite	Prt + Qtz + Pl + Bt	PT04 (N25°00′47″ E114°37′37″)
	Amphibole-bearing Alkali-feldspar granite	Prt + Qtz + Amph + Pl + Bt	PT01 (N24°56′54″ E114°43′25″)
			PT02 (N24°57′05″ E114°45′31″)
			PT03 (N24°57′39″ E114°43′59″)
	Syenite	Or + Cpx + Bt + Qtz	TB03 (N24°59′13″ E114°45′07″)
Huangbu body	Syenite	Or + Amph + Cpx + Qtz + Bt	QN01 (N24°46′20″ E114°29′52″)
Chebu body	Gabbro	Pl + Cpx + Opx + Amph + Bt + Mag + Qtz	DN01 (N24°50′30″ E115°02′10″)
Chenglong body	Gabbro	Amph + Pl + Bt + Mag + Cpx + Qtz	LN01 (N24°47′48″ E114°39′12″)
			LN02 (N24°47′47″ E114°39′11″)

Mineral abbreviation: Amph, amphibole; Bt, biotite; Cpx, clinopyroxene; Mag, magnetite; Ms, muscovite; Opx, orthopyroxene; Or, orthoclase; Prt, perthite; Pl, plagioclase; Qtz, quartz.

Table 2
Representative microprobe analyses of amphibole and clinopyroxene in the GSGA.

Sample	PT03					TB03					QN-1											
Lithology	Pitou amphibole-bearing alkali-feldspar granite					Tabei syenite					Huangbu syenite											
Mineral	Amp	Amp	Amp	Amp	Amp	Cpx	Cpx	Cpx	Cpx	Cpx	Cpx	Cpx	Cpx	Cpx	Cpx	Cpx	Cpx	Cpx	Cpx	Amp	Amp	Amp
Spot	1	2	3	4	5	6	7	8	9	10	11	12	13	14	15	16	17	18	19	20	21	22
Weight percent																						
SiO_2	40.79	40.43	39.45	40.22	39.75	47.65	48.10	48.94	47.81	49.00	50.41	49.58	49.95	50.37	50.08	49.67	50.54	49.79	50.37	43.50	40.28	44.45
TiO_2	1.84	1.73	1.21	1.62	1.52	0.76	1.15	0.18	1.48	0.31	0.40	0.44	0.46	0.49	0.45	0.32	0.22	0.38	0.47	1.17	3.08	1.07
Al_2O_3	8.20	8.23	9.01	8.09	8.66	1.81	1.49	0.95	1.29	1.77	0.94	0.90	0.95	0.90	1.04	0.73	0.58	1.00	1.06	5.26	9.62	4.89
FeO^T	30.89	31.46	32.04	31.77	31.83	35.72	36.25	32.58	36.49	32.68	18.89	19.85	19.69	19.23	18.12	20.49	17.75	18.71	17.33	32.41	26.40	32.13
MnO	0.30	0.36	0.56	0.35	0.53	0.74	0.87	0.82	1.19	0.60	0.99	1.21	1.11	1.15	1.23	1.30	1.04	1.12	1.09	1.20	0.86	1.19
MgO	2.14	2.10	1.14	1.68	1.23	2.17	2.77	2.88	2.07	3.30	7.58	6.57	7.11	7.10	7.78	5.92	8.09	7.02	8.44	2.27	4.39	2.58
CaO	10.40	10.49	10.33	10.49	10.46	7.94	6.48	10.43	6.19	10.38	20.85	20.84	20.82	20.77	20.66	20.66	21.30	20.70	20.96	9.41	10.34	9.15
Na_2O	2.23	2.04	1.89	2.24	1.97	1.53	1.21	1.12	1.33	1.26	0.46	0.49	0.45	0.56	0.53	0.54	0.49	0.59	0.63	2.51	2.50	2.38
K_2O	1.15	1.13	1.36	1.17	1.27	0.73	0.62	0.30	0.87	0.41	0.01	bd	0.03	0.01	0.01	0.02	bd	0.01	bd	0.98	1.52	0.87
F	0.66	0.58	0.36	0.55	0.35	0.22	0.21	0.13	0.26	0.23	nd	nd	nd	nd	nd	nd	nd	nd	nd	nd	nd	nd
Cl	0.36	0.35	0.60	0.33	0.48	0.11	0.05	0.07	0.06	0.08	nd	nd	nd	nd	nd	nd	nd	nd	nd	nd	nd	nd
Total	98.94	98.91	97.94	98.50	98.05	99.38	99.18	98.38	99.04	100.00	100.53	99.88	100.56	100.59	99.89	99.66	100.01	99.31	100.33	98.70	98.96	98.70
Oxygens	23	23	23	23	23	6	6	6	6	6	6	6	6	6	6	6	6	6	6	23	23	23
Atomic proportions																						
Si	6.54	6.48	6.42	6.51	6.46	1.98	2.01	2.04	2.01	2.00	1.96	1.95	1.95	1.96	1.95	1.97	1.96	1.96	1.94	6.89	6.29	6.98
Al	1.55	1.55	1.73	1.54	1.66	0.09	0.07	0.05	0.06	0.09	0.04	0.04	0.04	0.04	0.05	0.03	0.03	0.05	0.05	0.98	1.77	0.91
Fe^{3+}	0.44	0.62	0.67	0.47	0.52	0.08	0.00	0.00	0.00	0.02	0.05	0.07	0.07	0.05	0.06	0.06	0.07	0.06	0.08	0.80	0.42	0.90
Ti	0.22	0.21	0.15	0.20	0.19	0.02	0.04	0.01	0.05	0.01	0.01	0.01	0.01	0.01	0.01	0.01	0.01	0.01	0.01	0.14	0.36	0.13
Mg	0.51	0.50	0.28	0.41	0.30	0.13	0.17	0.18	0.13	0.20	0.44	0.39	0.41	0.41	0.45	0.35	0.47	0.41	0.49	0.54	1.02	0.60
Fe^{2+}	3.71	3.60	3.69	3.83	3.80	1.16	1.26	1.13	1.28	1.09	0.56	0.58	0.57	0.57	0.53	0.62	0.51	0.56	0.48	3.49	3.03	3.33
Mn	0.04	0.05	0.08	0.05	0.07	0.03	0.03	0.03	0.04	0.02	0.03	0.04	0.04	0.04	0.04	0.04	0.03	0.04	0.04	0.16	0.11	0.16
Ca	1.79	1.80	1.80	1.82	1.82	0.35	0.29	0.47	0.28	0.45	0.87	0.88	0.87	0.87	0.86	0.88	0.89	0.87	0.87	1.60	1.73	1.54
Na	0.69	0.63	0.60	0.70	0.62	0.12	0.10	0.09	0.11	0.10	0.03	0.04	0.03	0.04	0.04	0.04	0.04	0.05	0.05	0.77	0.76	0.73
K	0.24	0.23	0.28	0.24	0.26	0.04	0.03	0.02	0.05	0.02	bd	bd	bd	bd	bd	bd	bd	bd	bd	0.20	0.30	0.17
Cl	0.10	0.10	0.17	0.09	0.13	nd	nd	nd	nd	nd	nd	nd	nd	nd	nd	nd	nd	nd	nd	nd	nd	nd
F	0.33	0.29	0.18	0.28	0.18	nd	nd	nd	nd	nd	nd	nd	nd	nd	nd	nd	nd	nd	nd	nd	nd	nd

Note: bd = below detection limit. nd = not determined. Fe^{3+} in clinopyroxene calculated using the formula of Droop (1987). Ferric iron estimate and nomenclature of amphibole follows the scheme recommended by Leake et al. (1997).

dating and Hf-isotopes, and whole-rock major and trace element compositions. See Appendix A for analytical details.

3. Brief petrography and mineralogy

3.1. Longyuanba complex

The Longyuanba biotite granite is gray, medium- to coarse-grained with a porphyritic texture. Euhedral alkali feldspar occurs as phenocrysts, which is almost white-coloured on outcrops. The rock consists mainly of alkali feldspar (orthoclase), quartz, plagioclase (An_{20-23}) and biotite. Accessory minerals include titanite, apatite, and magnetite. Undulatory extinction is common in quartz grains, reflecting some post-crystallization deformation.

The Longyuanba two-mica granite is leucocratic, medium- to coarse-grained, rarely porphyritic with orthoclase as minor phenocrysts. It consists of plagioclase (~35%; An_{18-20}), orthoclase (~25%) and quartz (~30%) with subordinate muscovite (~6%) and biotite (~4%). Apatite and Fe–Ti oxides are common accessory phases.

The Dafengnao syenite is homogeneous, light pink, and medium-grained. It is dominated by perthitic alkali feldspar with minor microcline (~5%) and interstitial quartz (~3%). The main accessory phases are Fe–Ti oxides, epidote and apatite. Carbonate and chlorite are present as alteration products of mafic minerals.

3.2. Pitou complex

The alkali-feldspar granite of the Pitou complex is pinkish-gray, coarse-grained, and equigranular with no apparent preferred textural orientation. The rock is dominated by perthitic alkali feldspar and quartz with <10% plagioclase and <5% biotite (the sole mafic phase). Accessory minerals include magnetite, zircon and apatite.

Pitou amphibole-bearing alkali-feldspar granite is distinguished by amphiboles as the dominant mafic mineral phase. The rock is light-gray and coarse-grained, and is dominated by perthitic alkali feldspar (up to 60%) and quartz with <10% plagioclase and ~4% amphibole, biotite and allanite. Accessory minerals include magnetite, apatite and epidote. Amphibole and biotite are apparently late and fill the interstices between orthoclase and quartz. The amphiboles belong to the calcic group with $Ca_B>1.5$ (see Leake et al., 1997; Table 2; Fig. 2), and can be further classified as Ferro-edenite and hastingsite ($Mg/(Mg+Fe^{2+})=0.07–0.12$; $Si=6.42–6.54$ apfu).

The Tabei syenite is pinkish-gray and porphyritic with 20 to 25% orthoclase phenocrysts (~3 to 8 mm in size). The groundmass consists of fine-grained orthoclase (~50%), clinopyroxene (~20%), quartz (~3%) and biotite (~2%). Accessory phases include minor apatite, zircon and abundant magnetite. The pyroxene is anhedral and interstitial, and can be classified as augite and pigeonite, with a composition of Wo_{16-26} En_{7-11} Fs_{63-76} (Fig. 3).

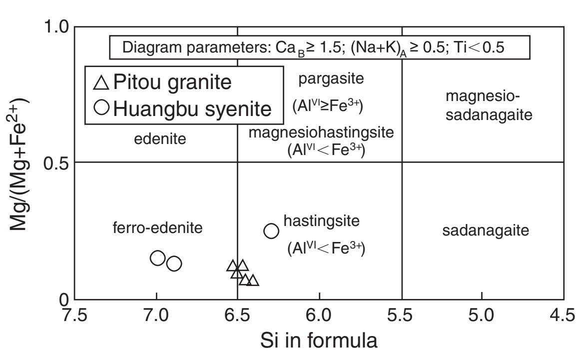

Fig. 2. Amphibole compositions from the Pitou amphibole-bearing alkali-feldspar granite and Huangbu syenite (after Leake et al., 1997).

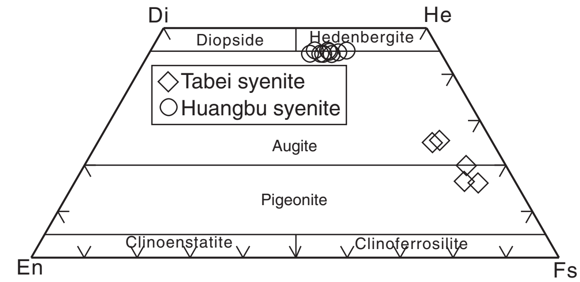

Fig. 3. Classification of pyroxene from the Tabei syenite and Huangbu syenite (after Morimoto et al., 1988).

3.3. Huangbu syenite

The rock is darkish-red and medium- to coarse-grained with a subhedral granular texture. It is dominated by orthoclase (~80%), amphibole (~10%), augite (~4%) and biotite (~3%). Small quantities of quartz occur as interstitial grains. Accessory phases include titanite, apatite and magnetite. Albite occurs locally as patches or veins in orthoclase, forming perthitic alkali feldspar. Amphibole is bright green and pleochroic with compositions of ferro-edenite and hastingsite ($Mg/[Mg+Fe^{2+}]=0.13–0.25$; $Si=6.29–6.98$ apfu) (Table 2; Fig. 2). Augite usually occurs as euhedral grains and ranges from augitic to hedenbergitic compositions (Wo_{44-45} En_{18-25} Fs_{31-37}) (Fig. 3). Contrary to the statements of Li et al. (2003) and Chen et al. (2005), our data show that there is a lack of sodic pyroxenes or sodic amphiboles, such as aegirine and riebeckite, in Tabei and Huangbu syenites and Pitou amphibole-bearing alkali-feldspar granite.

3.4. Chebu and Chenglong gabbros

The Chebu gabbro is dark-gray and shows a medium-grained gabbroic texture. It mainly consists of plagioclase (~55%; An_{60}) and clinopyroxene (30%) with subordinate amphibole, biotite, orthopyroxene and accessory Fe–Ti oxides and apatite. Quartz is less common and forms interstitial grains. Clinopyroxene forms mostly as subhedral to euhedral grains, and rarely as large poikilitic (up to 5 mm) crystals.

The Chenglong gabbro is melanocratic, fine-grained and contains abundant amphibole (~70%), subordinate plagioclase (~20%; An_{70}), minor biotite, titanomagnetite, clinopyroxene, titanite and quartz. Amphibole is mostly brown and minor green, and is subhedral to euhedral. The mineral assemblage is similar to the Xialan gabbro in the eastern Nanling region despite high proportions of Fe–Ti oxides (Yu et al., 2010). In both gabbroic bodies, the rock contains amphibole and plagioclase as essential minerals. The Chenglong gabbro exhibits typical cumulate textures, with euhedral amphibole, plagioclase and Fe–Ti oxides as cumulate phases up to 1–1.5 mm in length. Intercumulus minerals mainly include amphibole, biotite, plagioclase and quartz. The presence of ~15% intercumulus phases makes it more appropriate as mesocumulate (see Irvine, 1987).

4. Analytical results

4.1. Zircon U–Pb ages and Hf isotopic compositions

The localities of selected samples for LA-ICP-MS zircon U–Pb dating and Hf isotopic analysis are shown in Fig. 1b (also see Table 1). BSE images of representative zircons are shown in Fig. 4. The age results for samples of these intrusions are available in Electronic Data Table 1 and graphically shown in Fig. 5. The zircon Hf analyses were done on the same grains as used for U–Pb dating. Analytical results of the Lu–Hf isotopic compositions are given in Electronic Data Table 2 and illustrated in Fig. 6. We adopt model Hf ages as either T_{DM} when

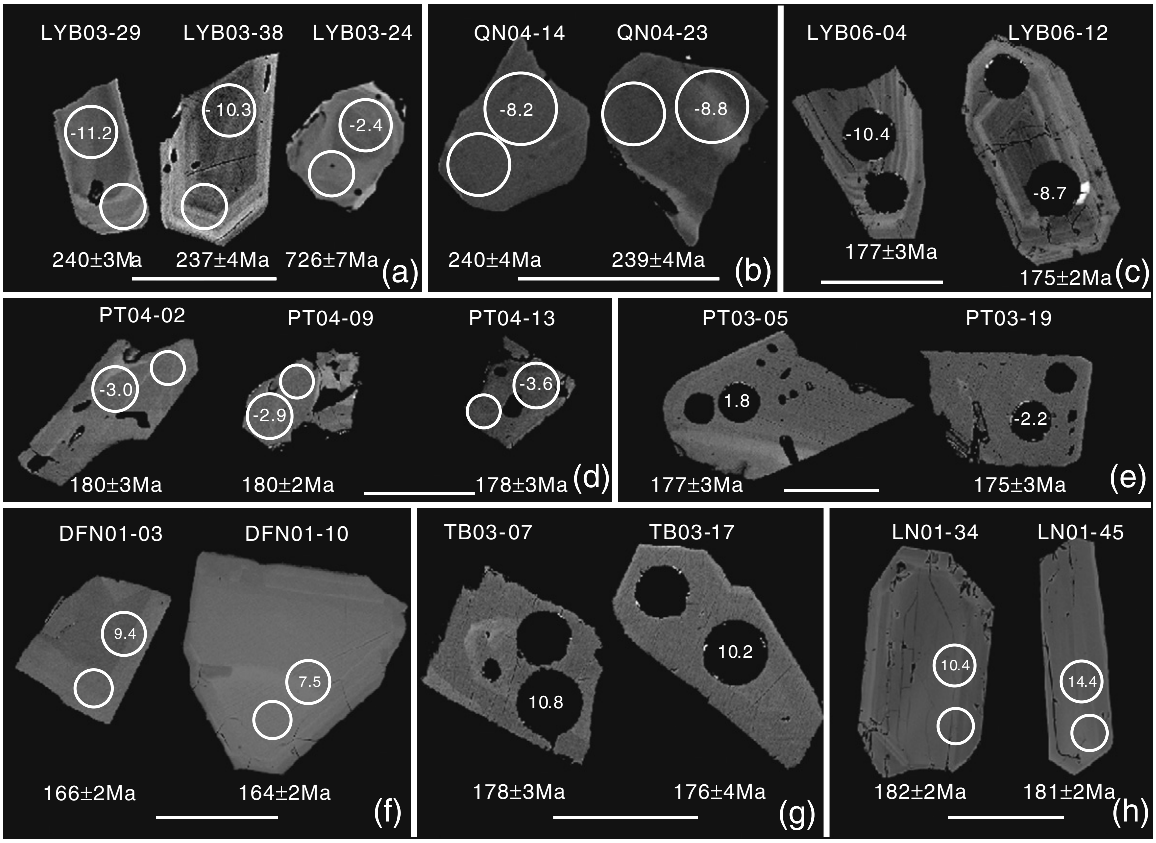

Fig. 4. Backscatter electron images of representative zircons from Longyuanba biotite granite (a, b) and two-mica granite (c), Pitou alkali-feldspar granite (d), Pitou amphibole-bearing alkali-feldspar granite (e), Dafengnao syenite (f), Tabei syenite (g), and Chenglong gabbro (h). Circles with enclosed data indicate the spots of Hf isotope analyses, whereas circles without data indicate the spots of U–Pb dating. The scale bar is 100 μm.

$\varepsilon_{Hf}(t)>0$ or T_{DM2} when $\varepsilon_{Hf}(t)<0$ in subsequent discussions (Zheng et al., 2007). In addition, we discuss the results according to rock types in sequence.

4.1.1. Longyuanba biotite granite

Two samples were selected from the Longyuanba biotite granite for analyses. Sample LYB03 is from the central part of the granite body. Zircons separated from this sample are euhedral and prismatic, up to 200 μm long, and have weak oscillatory zoning (Fig. 4a). They have highly variable abundances of Th (66–1219 ppm) and U (164–1663 ppm) and high Th/U ratios (from 0.19 to 2.21). Among the 22 U–Pb analyses, two zircons (LYB03–08 and LYB03–24) give older ages of 596 Ma and 726 Ma respectively, indicating that they are inherited. The remaining 20 analyses yield $^{206}Pb/^{238}U$ ages within analytical errors (237–245 Ma) with a weighted mean of 240.7 ± 1.4 Ma (MSWD = 0.45; Fig. 5a). Sample QN04 is from the eastern margin of the granite body. Zircons from this sample are similar to those from LYB03, but lack obvious oscillatory zoning (Fig. 4b). Twenty U–Pb analyses show variably high Th (151–1808 ppm), U (248–650 ppm), and Th/U (0.49–2.88), and yield a weighted mean $^{206}Pb/^{238}U$ age of 239.5 ± 1.4 Ma (MSWD = 0.31, Fig. 5b). This age is the same as that of LYB03 within error. So, the age of 240 Ma is interpreted as the best estimate of the crystallization age for the Longyuanba biotite granite, i.e., the intrusion was emplaced in the Middle Triassic.

Sixteen Hf isotopic spot analyses were obtained for LYB03. The main group of zircons with a $^{206}Pb/^{238}U$ age of ~240 Ma show varying initial $^{176}Hf/^{177}Hf$ ratios (0.282307 to 0.282393) or $\varepsilon_{Hf}(t)$ values (−8.1 to −11.2) with a weighted mean of −10.2 ± 0.5 (Fig. 6a), corresponding to T_{DM2} model ages of 1.79–1.98 Ga. One older zircon with age of 726 Ma has a $\varepsilon_{Hf}(t)$ value of −2.4 and T_{DM2} model age of 1.80 Ga. Zircon Hf isotopic compositions of QN04 show a significant overlap with those of LYB03 in both $\varepsilon_{Hf}(t)$ values and T_{DM2} model ages (Fig. 6b). Fifteen analyses yield a narrow range of initial $^{176}Hf/^{177}Hf$ ratios (0.282347 to 0.282420) or $\varepsilon_{Hf}(t)$ values (−7.2 to −9.9) with a weighted mean of −8.6 ± 0.4, corresponding to T_{DM2} ages of 1.73–1.89 Ga.

4.1.2. Longyuanba two-mica granite

Zircons from a representative sample (LYB06) are light brown and transparent, typically 150–230 μm long and 100–120 μm wide. Most zircon grains exhibit prismatic and pyramidal crystal faces with well-developed growth zoning (Fig. 4c). They have high and varying Th (240–4115 ppm), U (326–4045 ppm), and Th/U ratios (0.09 to 2.87). Of the 21 analyses, one grain (LYB06–03) records an older $^{206}Pb/^{238}U$ age of 525 ± 8 Ma. Four zircons record $^{206}Pb/^{238}U$ ages of ~240 Ma, which is the same as the emplacement age of Longyuanba biotite granite. These ~240 Ma zircon grains with sub-rounded shapes are considered to be introduced by wall-rock contamination during magma ascent, since the Longyuanba two-mica granite shows the relationship of intruding the biotite granite. The remaining 16 analyses plot on or in the vicinity of the concordia curve, and yield $^{206}Pb/^{238}U$ ages between 173 and 180 Ma. Fourteen concordant grains define a weighted mean $^{206}Pb/^{238}U$ age of 176.1 ± 1.5 Ma (MSWD = 0.68, Fig. 5c), which is taken as the crystallization age of the two-mica granite.

Fig. 5. Zircon U–Pb concordia diagrams and weighted mean $^{206}Pb/^{238}U$ ages for Longyuanba biotite granite (a and b) and two-mica granite (c), Pitou alkali-feldspar granite (d), Pitou amphibole-bearing alkali-feldspar granite (e), Dafengnao syenite (f), Tabei syenite (g), Huangbu syenite (h), Chebu gabbro (i) and Chenglong gabbro (h). The U–Pb isotope data of Huangbu syenite and Chebu gabbro are from He et al. (2007).

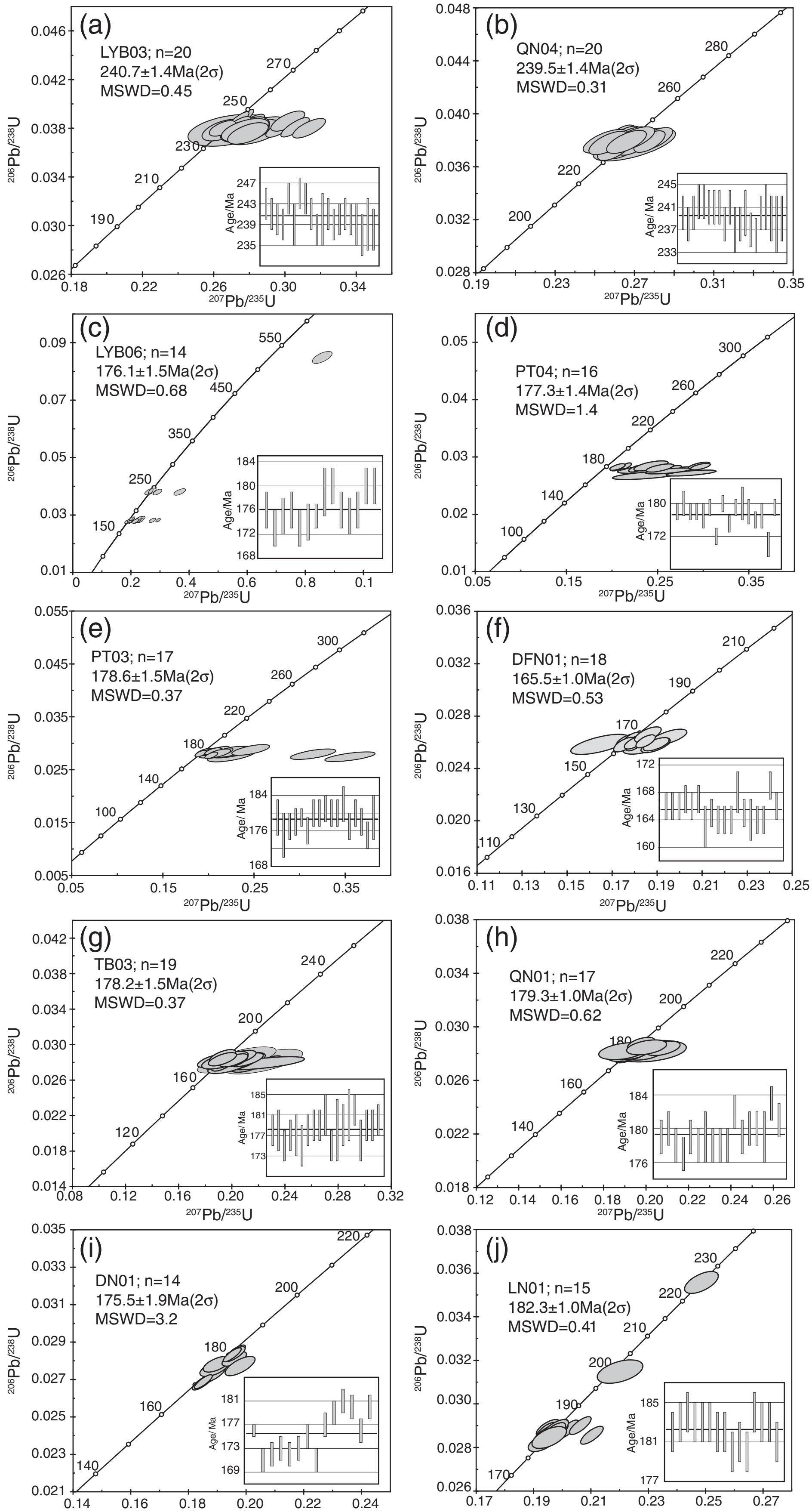

(a)
LYB03; n=20
240.7±1.4Ma(2σ)
MSWD=0.45
(b)
QN04; n=20
239.5±1.4Ma(2σ)
MSWD=0.31
(c)
LYB06; n=14
176.1±1.5Ma(2σ)
MSWD=0.68
(d)
PT04; n=16
177.3±1.4Ma(2σ)
MSWD=1.4
(e)
PT03; n=17
178.6±1.5Ma(2σ)
MSWD=0.37
(f)
DFN01; n=18
165.5±1.0Ma(2σ)
MSWD=0.53
(g)
TB03; n=19
178.2±1.5Ma(2σ)
MSWD=0.37
(h)
QN01; n=17
179.3±1.0Ma(2σ)
MSWD=0.62
(i)
DN01; n=14
175.5±1.9Ma(2σ)
MSWD=3.2
(j)
LN01; n=15
182.3±1.0Ma(2σ)
MSWD=0.41
^{206}Pb/^{238}U
^{207}Pb/^{235}U
Age/Ma

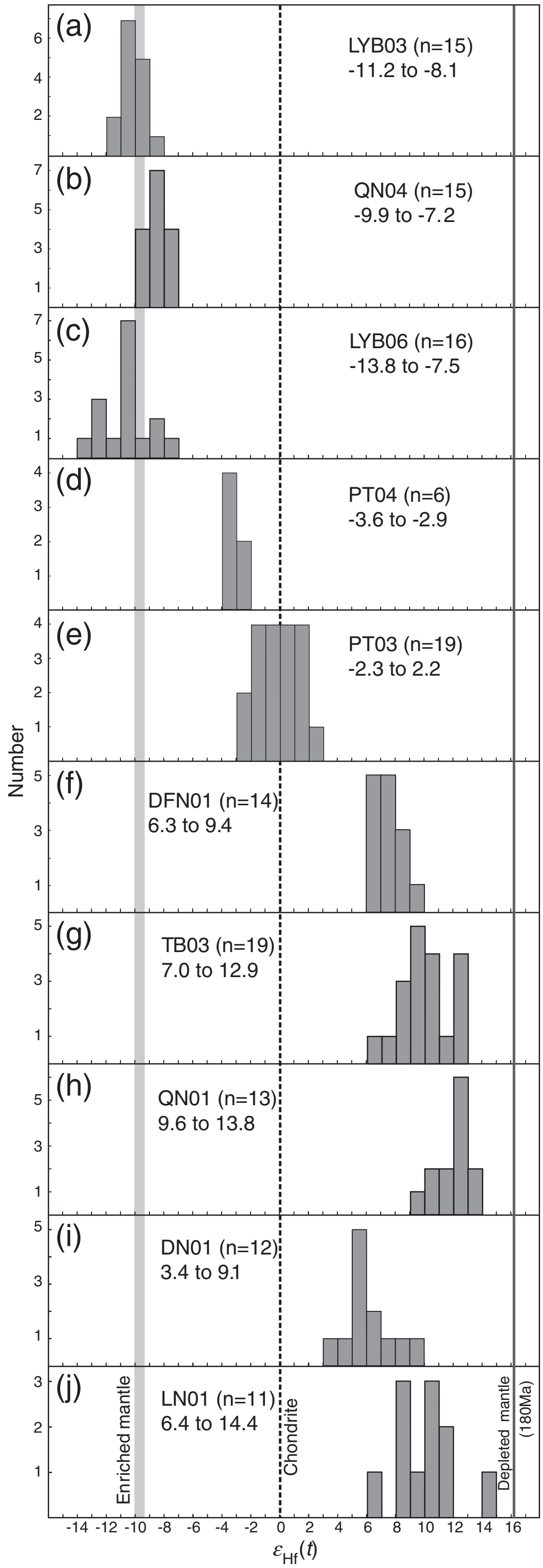

Fig. 6. Histograms of $\varepsilon_{Hf}(t)$ values for zircons from Longyuanba biotite granite (a and b) and two-mica granite (c), Pitou alkali-feldspar granite (d), Pitou amphibole-bearing alkali-feldspar granite (e), Dafengnao syenite (f), Tabei syenite (g), Huangbu syenite (h), Chebu gabbro (i), and Chenglong gabbro (j). The enriched mantle "composition" is represented by the Yangfang aegirite augite syenite in western Fujian (Wang et al., 2005a).

Two zircons with the age of ~240 Ma give $\varepsilon_{Hf}(t)$ values of −7.7 and −8.4 and T_{DM2} model age of 1.76 Ga and 1.80 Ga, confirming that they are xenocrystic zircons incorporated from the pre-existing country rock Longyuanba biotite granite. The main group of zircons with a $^{206}Pb/^{238}U$ age of ~176 Ma have varying initial $^{176}Hf/^{177}Hf$ ratios (0.282274 to 0.282450) or $\varepsilon_{Hf}(t)$ values (−7.5 to −13.8) with a weighted mean of −10.7 ± 0.9 (Fig. 6c), corresponding to T_{DM2} model ages between ~1.70 Ga and 2.09 Ga.

4.1.3. Pitou alkali-feldspar granite

Zircons from a representative sample (PT04) appear as grain fragments, up to 200 μm in length, with weak oscillatory zoning (Fig. 4d). Their high Th/U ratios (0.45 to 1.16) are consistent with the zircons being of magmatic origin. Sixteen analyses yield $^{206}Pb/^{238}U$ ages mostly between 170 and 180 Ma, with a weighted mean $^{206}Pb/^{238}U$ age of 177.3 ± 1.4 Ma (MSWD = 1.4, Fig. 5d). This age is interpreted as crystallization age of Pitou alkali-feldspar granite. Six analyses of Hf isotopic compositions give a weighted mean $\varepsilon_{Hf}(t)$ values of −3.3 ± 0.6 (Fig. 6d), and T_{DM2} model age of 1.43 ± 0.04 Ga.

4.1.4. Pitou amphibole-bearing alkali-feldspar granite

Zircons from sample PT03 are transparent, light yellow, larger than those from amphibole-barren alkali-feldspar granite (sample PT04) (Fig. 4e). Nineteen analyses for 19 zircons from this sample yield varying Th/U ratios (0.31 to 2.90), and give $^{206}Pb/^{238}U$ ages between 174 and 182 Ma. Seventeen concordant analyses give a weighted mean $^{206}Pb/^{238}U$ age of 178.6 ± 1.5 Ma (MSWD = 0.37, Fig. 5e), which is taken as the crystallization age for Pitou amphibole-bearing alkali-feldspar granite. These zircons show a wide range of Hf isotopic compositions with varying initial $^{176}Hf/^{177}Hf$ ratios (0.282599 to 0.282725) or $\varepsilon_{Hf}(t)$ values (−2.3 to 2.2) with a weighted mean of 0 ± 0.7 (Fig. 6e), corresponding to T_{DM2} model ages of 1.08 to 1.37 Ga.

4.1.5. Dafengnao syenite

Zircons in sample DFN01 are euhedral, stubby, prismatic, and are 100–150 μm in size, with some oscillatory zoning (Fig. 4f). Thirty analyses on 30 zircons show varying Th (212–4476 ppm), U (247–1983 ppm) and Th/U ratios (0.86–3.15). The bulk of the analyses (n = 18) is tightly grouped and concordant, defining a weighted mean $^{206}Pb/^{238}U$ age of 165.5 ± 1.0 Ma (MSWD = 0.53, Fig. 5f), which is interpreted as the crystallization age of the Dafengnao syenite. Fourteen zircons yield a limited range of initial $^{176}Hf/^{177}Hf$ ratios (0.282848 to 0.282936) or $\varepsilon_{Hf}(t)$ values (6.3 to 9.4) with a weighted mean of 7.7 ± 0.6 (Fig. 6f), corresponding to T_{DM} model ages of 0.44 Ga to 0.59 Ga.

4.1.6. Tabei syenite

Zircons from sample TB03 are mostly of stubby/euhedral shape, pale brown, up to 180 μm in size, and generally have oscillatory zoning (Fig. 4g). A total of 19 analyses on 19 grains give high and varying Th (108–1435 ppm), U (129–1255 ppm) and Th/U (0.59–1.68). All the analyses are concordant or nearly so, giving $^{206}Pb/^{238}U$ ages of 175–182 Ma. A weighted mean age of 178.2 ± 1.5 Ma (MSWD = 0.37, Fig. 5g) is interpreted as the crystallization age of this syenite. These zircons show varying initial $^{176}Hf/^{177}Hf$ ratios (0.282857 to 0.283027) or $\varepsilon_{Hf}(t)$ values (7.0 to 12.9) with a weighted mean of 10.0 ± 0.8 (Fig. 6g), corresponding to T_{DM} model ages of 0.31 Ga to 0.57 Ga.

4.1.7. Huangbu syenite

The zircon U–Pb age data for Huangbu syenite (sample QN01) have been described in detail by He et al. (2007). Eighteen analyses of zircons from this sample yield $^{206}Pb/^{238}U$ ages of 178–183 Ma, with a weighted mean age of 179.3 ± 1.0 Ma (MSWD = 0.62, Fig. 5h). Thirteen zircons yield varying initial $^{176}Hf/^{177}Hf$ ratios (0.282935 to 0.283051) or $\varepsilon_{Hf}(t)$ values (9.6 to 13.8) with a weighted mean of 12.4 ± 0.7 (Fig. 6h), corresponding to T_{DM} model ages of 0.28 Ga to 0.45 Ga.

4.1.8. Chebu gabbro

A zircon U–Pb age of 175.5 ± 1.9 Ma has been reported by He et al. (2007) for Sample DN01 of the Chebu gabbro (Fig. 5i). These same zircon grains were analyzed for Hf isotopic compositions, giving varying initial $^{176}Hf/^{177}Hf$ ratios (0.282761 to 0.282922) or $\varepsilon_{Hf}(t)$ values (3.4 to 9.1) with a weighted mean of 6.0 ± 1.0 (Fig. 6i), corresponding to T_{DM} model ages of 0.48 Ga to 0.72 Ga.

4.1.9. Chenglong gabbro

Zircons from the sample LN01 are mostly euhedral, up to 200 μm in size. Most crystals are transparent and light brown. Euhedral concentric zoning is common in most crystals (Fig. 4h). A total of 19 analyses on 19 zircons give varying Th/U ratios (0.36 to 2.74). Seventeen analyses are tightly clustered on or nearby the concordia curve, yielding $^{206}Pb/^{238}U$ ages of 180 to 184 Ma. Fifteen concordant grains define a weighted mean $^{206}Pb/^{238}U$ age of 182.3 ± 1.0 Ma (MSWD = 0.41, Fig. 5j), which gives the best estimate of the crystallization age of the Chenglong gabbro. Two grains (LN01–07 and LN01–37) record older $^{206}Pb/^{238}U$ ages of 225 and 200 Ma. These reflect the incorporation of xenocrystic zircons, probably incorporated from slightly older crust during ascent of the magma.

Eleven zircons with a $^{206}Pb/^{238}U$ age of ~182 Ma have been analyzed for Hf isotopic compositions, yielding varying initial $^{176}Hf/^{177}Hf$ ratios (0.282839 to 0.283067) or $\varepsilon_{Hf}(t)$ values (6.4 to 14.4) with a weighted mean of 10.0 ± 1.3 (Fig. 6j), corresponding to T_{DM} model ages of 0.26 Ga to 0.59 Ga.

4.2. Major and trace element characteristics

A complete data set of bulk-rock major and trace element analyses for representative samples from the GSGA and some previously

Table 3
Representative chemical compositions of samples from the GSGA.

Sample	LYB03	LYB06	PT01	PT04	DFN01	9702-1[a]	QN01	DN01	DN02	LN01	LN02
	LBG	LTMG	PABAG	PAG	DS	TS	HS	CBG		CLG	
Major elements (in wt.%)											
SiO_2	72.49	74.24	72.68	77.34	64.11	62.4	61.29	48.72	47.75	43.56	44.93
TiO_2	0.33	0.26	0.21	0.14	0.37	0.29	0.59	1.65	1.64	4.31	4.05
Al_2O_3	12.98	13.74	13.44	11.21	15.21	18.07	16.82	16.37	16.95	11.66	12.13
FeO^T	2.56	1.61	2.65	1.49	4.99	4.48	6.18	11.65	11.70	18.29	17.67
MnO	0.05	0.03	0.06	0.03	0.12	0.1	0.22	0.15	0.14	0.18	0.18
MgO	0.81	0.38	0.01	0.00	0.14	0.28	0.63	8.16	7.62	7.17	6.77
CaO	2.15	0.30	0.78	0.57	1.88	0.8	1.82	8.35	8.76	11.27	10.38
Na_2O	2.31	2.76	3.27	2.62	4.94	6.44	5.45	2.72	2.74	2.45	2.51
K_2O	4.76	5.61	6.10	5.11	6.06	5.52	6.00	0.96	0.70	0.63	0.88
P_2O_5	0.15	0.15	0.03	0.02	0.04	0.16	0.12	0.32	0.28	0.39	0.44
LOI	0.90	0.99	0.30	1.08	1.96	1.04	0.78	1.20	2.08	1.07	1.03
Total	99.48	100.06	99.55	99.61	99.81	99.90	99.90	100.24	100.36	100.98	100.95
A/CNK	1.01	1.23	1.00	1.03	0.84	1.00	0.90	0.79	0.80	0.46	0.51
A/NK	1.45	1.29	1.12	1.14	1.03	1.09	1.09	2.97	3.22	2.47	2.39
Trace elements (in ppm)											
V	35.0	17.4	10.4	8.3	7.66	–	2.16	174	187	543	502
Cr	17.4	6.76	5.83	3.91	27.6	–	13.62	55.9	90	18.36	14.49
Ni	9.41	4.33	4.07	1.78	11.5	–	5.70	122	99	79.7	65.2
Ga	16.3	22.5	26.7	21.0	36.7	23.1	22.4	19.4	19.6	23.2	23.3
Rb	267	384	142	295	103	123	114	51.4	42.4	20.8	30.8
Sr	209	80.8	33.2	29.1	46.1	142	60.4	326	320	404	463
Y	20.5	12.6	29.7	48.8	14.3	19.5	33.7	30.5	27.3	31.8	33.5
Zr	240	163	571	178	138	536	419	190	169	193	222
Nb	16.4	16.3	35.9	27.5	29.0	120	76.0	24.4	21.5	26.2	28.3
Ba	495	375	300	213	177	706	1345	171	143	173	194
Hf	7.61	4.74	13.5	6.20	3.61	9.99	10.1	5.22	4.91	5.86	6.25
Ta	1.75	2.78	3.13	4.44	1.84	6.35	4.21	1.80	1.55	1.78	1.91
Pb	83.4	38.3	23.9	28.9	13.9	–	11.01	7.15	8.90	5.00	4.40
Th	47.5	36.7	25.2	26.8	3.96	9.8	4.44	7.15	6.97	2.15	2.37
U	13.5	8.62	3.09	8.32	1.15	2.5	1.49	1.88	1.88	0.67	0.67
La	61.6	58.1	131	54.5	26.3	55.7	40.7	22.7	19.5	20.9	24.4
Ce	111	116	262	108	54.2	87.7	88.8	48.5	42.0	51.7	57.2
Pr	13.6	12.8	27.5	12.3	6.81	8.77	11.2	5.98	5.28	7.09	7.76
Nd	47.0	45.9	96.3	44.1	26.7	27.6	42.5	25.3	21.5	32.8	34.7
Sm	7.96	7.62	15.3	9.18	5.41	4.32	8.59	5.45	5.26	7.85	8.28
Eu	1.16	0.74	1.67	0.58	1.29	0.84	2.92	1.39	1.45	2.28	2.42
Gd	5.49	4.96	10.9	8.04	4.53	3.61	7.04	5.25	4.75	6.99	7.47
Tb	0.86	0.49	1.15	1.20	0.54	0.52	1.30	1.05	0.96	1.33	1.40
Dy	3.87	2.48	6.77	8.21	3.49	3.05	6.63	5.71	5.18	6.47	6.85
Ho	0.73	0.43	1.28	1.75	0.67	0.58	1.27	1.21	1.07	1.27	1.32
Er	2.00	1.12	3.48	5.28	1.87	1.71	3.44	2.98	2.74	2.92	3.00
Tm	0.37	0.15	0.48	0.75	0.26	0.29	0.66	0.57	0.52	0.49	0.52
Yb	2.21	0.91	3.07	4.73	1.75	2.09	3.99	3.40	3.07	2.84	2.87
Lu	0.32	0.13	0.50	0.71	0.31	0.35	0.59	0.42	0.41	0.34	0.36
Eu/Eu*	0.51	0.34	0.38	0.20	0.78	0.63	1.12	0.79	0.87	0.92	0.92
$[La/Yb]_{CN}$	18.79	42.94	28.91	7.77	10.14	18.01	6.89	4.52	4.30	4.97	5.75
∑REE	258.33	251.81	561.25	258.97	134.11	197.13	219.69	129.96	113.70	145.29	158.52

Note: LOI: loss on ignition. $Eu/Eu^* = 2 \times Eu_N/(Sm_N + Gd_N)$; $A/CNK = Al_2O_3/[CaO + Na_2O + K_2O]$ (mol%); $A/NK = Al_2O_3/[Na_2O + K_2O]$ (mol%); Abbreviations: LBG—Longyuanba biotite granite; LTMG—Longyuanba two-mica granite; PABAG—Pitou amphibole-bearing alkali-feldspar granite; PAG—Pitou alkali-feldspar granite; DS—Dafengnao syenite; TS—Tabei syenite; HS—Huangbu syenite; CBG—Chebu gabbro; CLG—Chenglong gabbro.

[a] Data from Chen et al. (2005).

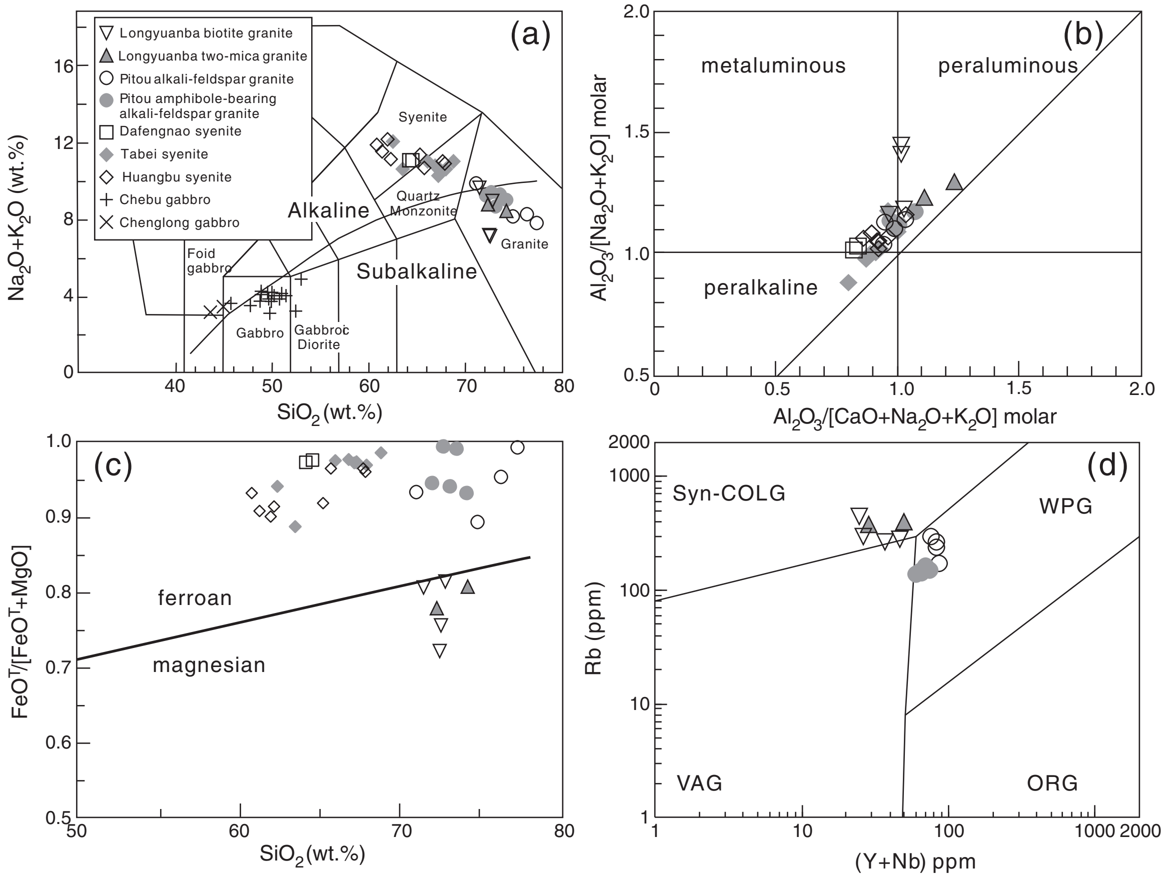

Fig. 7. (a) The total alkali vs. silica (TAS) diagram (after Middlemost, 1994) used for the classification of the GSGA samples. (b) Chemical compositions of felsic units of the GSGA in terms of alumina saturation. (c) $FeO^T/[FeO^T+MgO]$ vs. SiO_2 diagram for felsic units of the GSGA (after Frost et al., 2001). (d) Rb vs. (Y + Nb) discrimination diagram after Pearce et al. (1984). Abbreviations: VAG, volcanic arc granites; syn-COLG, syn-collisional granites; ORG, ocean ridge granites; WPG, within-plate granites.

published data are listed in Electronic Data Table 3, and an abbreviated version with representative analyses is provided in Table 3.

All the granite samples of the GSGA show high SiO_2 (between 71.44 and 77.34 wt.%), and plot in the granite field on the total alkali-silica (TAS) diagram (Fig. 7a). These rocks have relatively high total alkalis with K_2O+Na_2O ranging from 7.07 to 9.80 wt.%. Fig. 7b shows the compositions of the granites in terms of their molar ratios of $Al_2O_3/[CaO+Na_2O+K_2O]$ (A/CNK) and $Al_2O_3/[Na_2O+K_2O]$ (A/NK). Based on these ratios, the Longyuanba biotite granites and two-mica granites are peraluminous (A/CNK = 1.01–1.23) except for one Longyuanba biotite granite sample that is metaluminous (0.96), whereas the Pitou alkali-feldspar granites and amphibole-bearing alkali-feldspar granites straddle the boundary between metaluminous and weakly peraluminous (A/CNK = 0.94–1.07). Following Frost et al. (2001) (Fig. 7c), the Longyuanba biotite granites and two-mica granites belong to magnesian granites with low $FeO^T/[FeO^T+MgO]$ (0.73–0.82). In contrast, the Pitou alkali-feldspar granites and amphibole-bearing alkali-feldspar granites are rich in iron relative to Mg with high $FeO^T/[FeO^T+MgO]$ (0.90–1.00), and plot in the broad field of ferroan granites (see Frost et al., 2001). In the Rb vs. (Y + Nb) plot (Fig. 7d), the Longyuanba biotite granites and two-mica granites fall in the syn-collisional granite field, whereas the Pitou alkali-feldspar granites and amphibole-bearing alkali-feldspar granites are assigned to the within-plate granite field.

Both high and low $FeO^T/[FeO^T+MgO]$ granites show similar chondrite-normalized REE patterns with relative enrichment of LREE over HREE and significant negative Eu anomalies (Fig. 8a). The $[La/Yb]_{CN}$ values are higher in Longyuanba biotite granites and two-mica granites (19–43) than in Pitou alkali-feldspar granites (8–14). The Pitou amphibole-bearing alkali-feldspar granites have highest total REE ($\sum REE = 429$–718 ppm), higher than both Longyuanba biotite/two-mica granites and Pitou alkali-feldspar granites, and have a uniform $[La/Yb]_{CN}$ (24–30). In the primitive mantle-normalized trace element diagram (Fig. 8b), they are all characterized by negative Ba, Nb and Ta anomalies and marked depletion in Sr, P and Ti. But the Pitou amphibole-bearing alkali-feldspar granites are distinctly more enriched in HFSE (i.e., Nb, Zr and Hf) and LREEs (i.e., La, Ce, Nd and Sm) than other granites.

The Huangbu, Tabei and Dafengnao syenites are silica over-saturated rocks containing quartz, with varying SiO_2 (60.79 to 68.75 wt.%). They all have high K_2O+Na_2O (10.19–12.08 wt.%), and plot in the alkaline field on the TAS diagram (Fig. 7a). Most of these samples are metaluminous (Fig. 7b), while three samples of Tabei syenite are peralkaline with lower A/NK values (0.88–0.98). They all show high K, plotting in the shoshonite field in both K_2O–SiO_2 and K_2O–Na_2O diagrams (Fig. 9). All the three syenite bodies show variably elevated REE abundances but similar REE patterns with $[La/Yb]_{CN}$ values ranging from 5 to 18 (Fig. 8c). Also, they display distinct negative or positive Eu anomalies (Eu/Eu^*: 0.30 to 1.82), which likely reflect fractionation or accumulation of plagioclase feldspar. On primitive mantle-normalized trace element diagrams, these syenites show enrichments in some elements such as K, Nb, Ta, Zr and Hf, but depletion in Sr, P and Ti, which are distinctly different from the Triassic Yangfang aegirite augite syenite in western Fujian (Fig. 8d). They also exhibit large variations in trace element abundances, particularly for Rb, Ba, Th, U, Nb and Ta in Huangbu and Tabei syenites characterized by positive or negative anomalies relative to other similarly incompatible trace elements (e.g., Nb vs. Th and Ta vs. U). The Tabei syenite lacks positive Pb anomaly, which is conspicuous in both Huangbu and Dafengnao syenites.

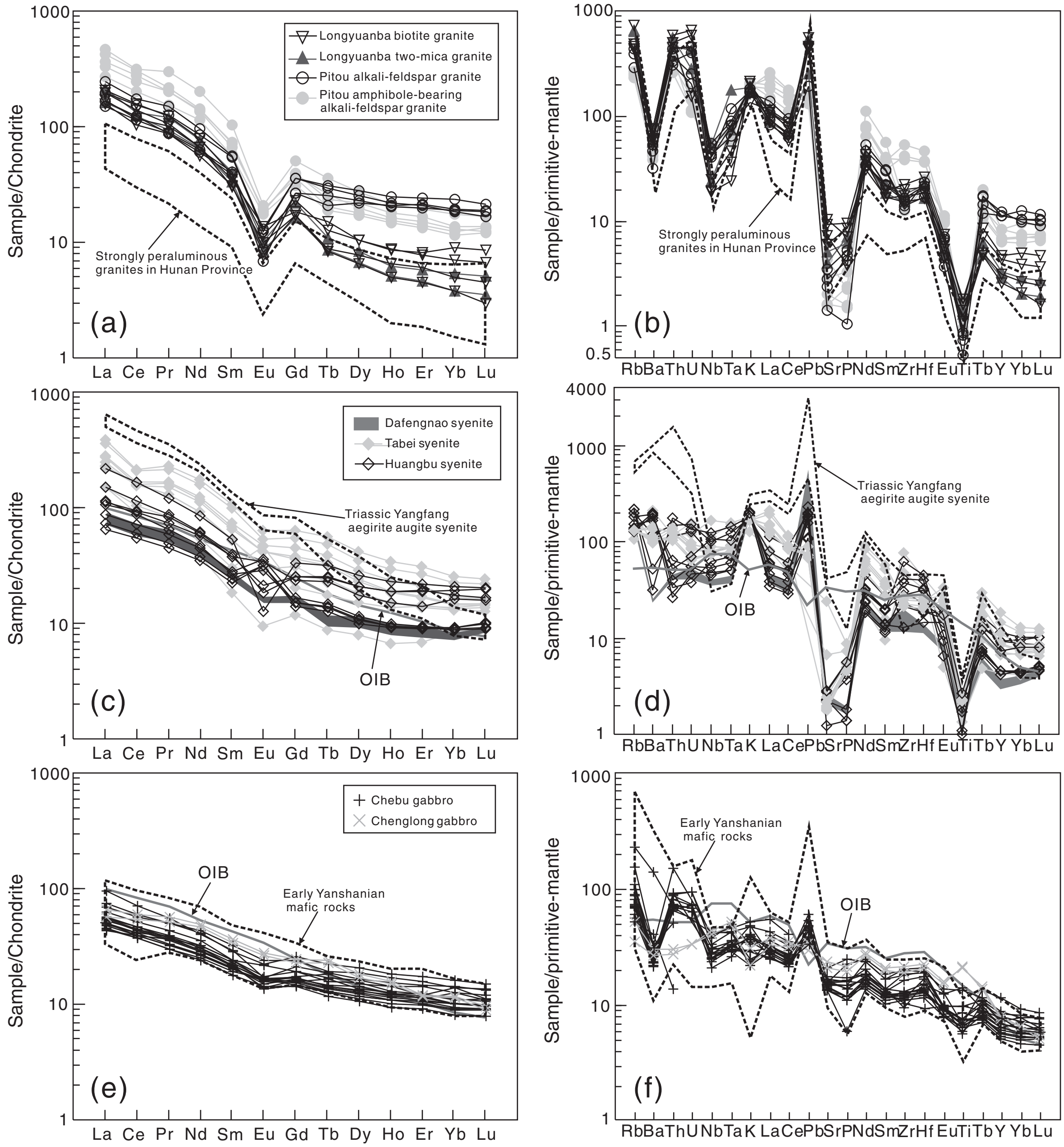

Fig. 8. Chondrite-normalized REE patterns (a, c and e) and Primitive mantle-normalized multiple trace element diagrams (b, d and f) for the granites, syenites and gabbros of the GSGA. The chondrite values are from Taylor and McLennan (1985). The primitive mantle values and the average ocean island basalt (OIB) composition are from Sun and McDonough (1989). Data for strongly peraluminous granites in Hunan Province (Wang et al., 2007b) and Triassic Yangfang aegirite augite syenite in western Fujian (Wang et al., 2005a) as well as Early Yanshanian mafic rocks in South China (Wang et al., 2003, 2005b; Yu et al., 2010) are also shown for comparison.

Samples of Chebu and Chenglong gabbros both contain quartz. The Chebu gabbros have higher SiO_2 (45.65–52.91 wt.%) than Chenglong gabbros (43.56–44.93 wt.%) likely because of Ti–Fe oxide accumulation and data closure effect (see Table 3). On the TAS diagram (Fig. 7a), most of the Chebu gabbros fall within the subalkaline field. However, the Chenglong gabbros plot in the alkaline field because of their low SiO_2. They all have low K_2O (0.62–1.50 wt.%) and very low K_2O/Na_2O (<0.5) (Fig. 9). Their variably high MgO (4.98–8.16 wt.%), FeO^T (7.41–18.29 wt.%), Ni (65.2–141 ppm) and Cr (14.5–89.8 ppm) are consistent with their mafic nature and with their being derived/evolved from mantle melts (Wilkinson and Le Maitre, 1987). They have high total REEs (93–170 ppm), and light REE enrichment (i.e., $[La/Sm]_{CN}>1$) with small to negligible Eu anomalies (Eu/Eu^*: from 0.68 to 1.01 for Chebu gabbros and 0.92 for Chenglong gabbros) (Fig. 8e). Their primitive mantle-normalized trace element systematics (Fig. 8f) resemble, to a certain extent, ocean island basalts (OIB) although we are aware that gabbros may not be melt, but cumulate and they can have melt-like (but not melt) compositions because of incompatible element concentration in trapped interstitial melt (Niu et al., 2002). Nevertheless, the Chebu gabbros have higher Th, U and Pb and lower Nb and Ta than OIB, suggesting the possibility that they may have derived from OIB-like mantle melt with the latter being mixed with a high Th, low Nb magma or contaminated by crustal material. Small anomalies in Ba, Sr, P and Eu are consistent with these rocks being cumulate (e.g., the effect of fractionation/accumulation of plagioclase and apatite).

4.3. Sr and Nd isotopic compositions

Sr and Nd isotope data for whole-rock samples of the GSGA are given in Table 4. Fig. 10 shows the data in $\varepsilon_{Nd}(t)$ vs. $[^{87}Sr/^{86}Sr]_i$ space.

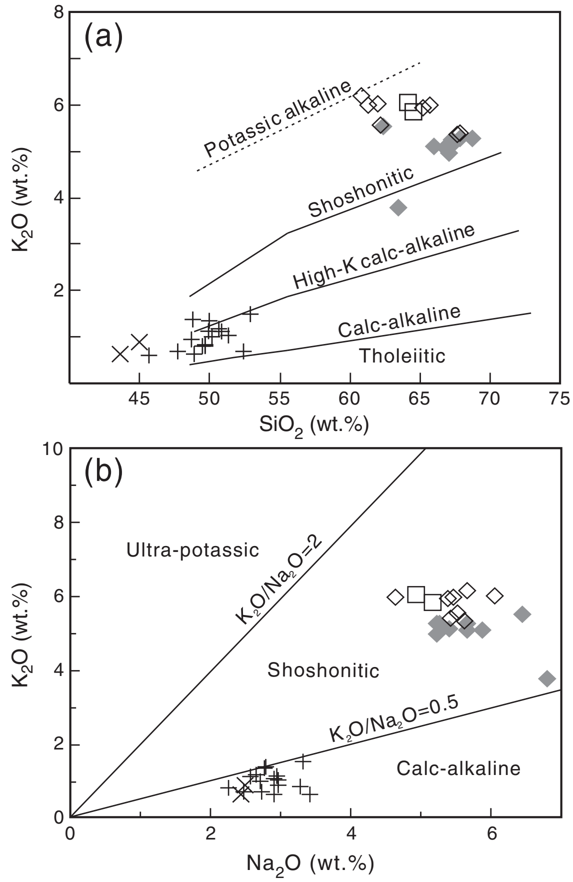

Fig. 9. Bulk-rock compositions of intermediate and mafic rocks from the GSGA plotted in (a) SiO_2 vs. K_2O (after Peccerillo and Taylor, 1976), where dashed line represents the division between potassic alkaline and shoshonitic suites (after Calanchi et al., 2002); and (b) K_2O vs. Na_2O (after Turner et al., 1996) variation diagrams. Symbols are same as in Fig. 7.

The Longyuanba biotite granite and two-mica granite have very similar Sr and Nd isotopic compositions with $[^{87}Sr/^{86}Sr]_i$ ranging from 0.71777 to 0.72910, $\varepsilon_{Nd}(t)$ from −12.0 to −13.7, and T^{Nd}_{DM2} from 1.98 to 2.08 Ga. These data are comparable with those from Triassic Darongshan cordierite granites (Hsieh et al., 2008) and Indosinian strongly peraluminous granites in Hunan Province (Wang et al., 2007b), which are typical Mesozoic S-type granitoids in South China. The initial $^{87}Sr/^{86}Sr$ ratios are ~0.70978–0.70980 for the Pitou alkali-feldspar granites, and ~0.70888 for the Pitou amphibole-bearing alkali-feldspar granites. The $\varepsilon_{Nd}(t)$ values of Pitou alkali-feldspar granites range from −5.4 to −6.4, and about −4.2 for the Pitou amphibole-bearing alkali-feldspar granites. These rocks have relatively younger T^{Nd}_{DM2} ages of ~1.5 Ga and 1.3 Ga, respectively.

The Chenglong gabbro has the highest $\varepsilon_{Nd}(t)$ value (+5.2) within the GSGA and low initial $^{87}Sr/^{86}Sr$ ratio of 0.70476. The Chebu gabbros have relatively lower $\varepsilon_{Nd}(t)$ values of −0.8 to 1.0 and higher $[^{87}Sr/^{86}Sr]_i$ ratios of 0.70645 to 0.70820. The Dafengnao, Tabei and Huangbu syenites have similar Sr–Nd isotopic compositions (Fig. 10). They have large variations in both $[^{87}Sr/^{86}Sr]_i$ (0.70279–0.71076) and $\varepsilon_{Nd}(t)$ (0.1–3.6). Some samples show no anticipated inverse $[^{87}Sr/^{86}Sr]_i$ vs. $\varepsilon_{Nd}(t)$ correlation (Fig. 10), which could be caused by post-emplacement mobilization of Sr (Li et al., 2003), but are more likely inherited from magma sources and source histories. Overall, the Sr–Nd isotopic compositions of these gabbroic and syenitic rocks can be compared with those of the Early Yanshanian mafic rocks in South China (Xie et al., 2006; Chen et al., 2008b; Wang et al., 2003, 2005b, 2008b; Yu et al., 2010) (Fig. 10).

5. Discussion

5.1. Genetic type of the granites

The four granite units (i.e., the Longyuanba biotite granites and two-mica granites; the Pitou alkali-feldspar granites and amphibole-bearing alkali-feldspar granites) all have high $10^4\times Ga/Al$ and high $Zr+Nb+Ce+Y$, and plot in the field of A-type granite in general (Whalen et al., 1987; Fig. 11a and b). It should be noted, however, that these discrimination diagrams are ineffective for highly evolved granites, which typically have higher values of these parameters (Eby, 1992; King et al., 2001). Nevertheless, distinctions among the four granite units do exist in important aspects:

(1) The $10^4\times Ga/Al$ of Pitou alkali-feldspar granites and Longyuanba biotite granites and two-mica granites show a scattered yet increasing trend with increasing Rb, whereas the Pitou amphibole-bearing alkali-feldspar granites have high $10^4\times Ga/Al$ but low Rb (Fig. 11c). This is consistent with varying extents of fractionation for the former three granite units whether they are I- or S-types. In contrast, the A-type-like characteristics of Pitou amphibole-bearing alkali-feldspar granites may be primary.
(2) The decreasing Eu/Eu* (or negative Eu anomalies) with decreasing Sr is consistent with feldspar removal, especially plagioclase, during magma evolution (Niu and O'Hara, 2009) for all granite units with the exception of 3 Pitou amphibole-bearing alkali-feldspar granite samples (Fig. 11d).
(3) The Longyuanba biotite granites and two-mica granites have high P_2O_5, whereas Pitou alkali-feldspar granites have low P_2O_5, which decreases further with increasing SiO_2 or extent of fractionation (i.e., apatite removal; Fig. 11e). This is an important criterion to distinguish between I-type and S-type granites for highly evolved samples (Chappell, 1999).
(4) The Pitou alkali-feldspar granites have very high Y (from 48.8 to 53.5 ppm), whereas the Longyuanba biotite granites and two-mica granites have substantially lower Y (11.4 to 20.5 ppm; Fig. 11f). These are also consistent with the anticipated differences between I- and S-type granites for highly evolved samples. We expect that low Y (hence low HREEs or high $[La/Yb]_N$ and $[Sm/Yb]_N$; Fig. 8a) of highly evolved S-type granite is consistent with the removal of garnet as a liquidus phase during early stage of S-type granite evolution.

On the other hand, the four granite units are very different in their mineralogy, especially in mafic minerals (Table 1). The Longyuanba biotite granite and two-mica granite contain biotite ± muscovite as Al-rich minerals. In the alkali-feldspar granite of the Pitou complex, feldspars are mainly perthitic alkali feldspar. Whereas Pitou amphibole-bearing alkali-feldspar granite contains amphiboles as the dominant mafic mineral phase, and late amphibole and biotite are found filling the interstices between orthoclase and quartz. Integrating these petrographic distinctions with geochemical differences, we conclude that the Longyuanba biotite granites and two-mica granites are evolved S-type granites, whereas the Pitou alkali-feldspar granites are evolved I-type granites. As to the Pitou amphibole-bearing alkali-feldspar granites, we propose that they could be classified as A-type granites. Furthermore, they have high Nb, Ta, and low in Y/Nb ratios (0.83–1.14), thus can be further classified as A_1-type granites (Y/Nb<1.2) according to Eby (1992).

5.2. Origin of the S-type granite units and the nature of the western Cathysia crust

As discussed above, the Longyuanba biotite granite and two-mica granite are best interpreted as S-type granite despite their different emplacement ages. Furthermore, their S-type affinity is confirmed by

Table 4
Sr and Nd isotopic compositions of samples from the GSGA.

Sample	Age (Ma)	Rb(ppm)	Sr(ppm)	$^{87}Rb/^{86}Sr$	$^{87}Sr/^{86}Sr$	2σ	$(^{87}Sr/^{86}Sr)_i$	Sm(ppm)	Nd(ppm)	$^{147}Sm/^{144}Nd$	$^{143}Nd/^{144}Nd$	2σ	$\varepsilon_{Nd}(t)$	T_{DM}(Ga)	T^{Nd}_{DM2} (Ga)
Longyuanba biotite granite															
YQ-7[a]	240	294	149	5.614	0.736933	11	0.71777	6.87	46.8	0.0920	0.511861	12	−12.0	1.61	1.98
YQ-43[a]	240	445	123	9.815	0.751658	11	0.71815	6.98	39.5	0.1116	0.511829	11	−13.2	1.97	2.08
Longyuanba two-mica granite															
YQ-57[a]	176	403	102	12.37	0.760051	12	0.72910	9.29	54.6	0.1079	0.511833	11	−13.7	1.89	2.08
Pitou alkali-feldspar granite															
9704-1[b]	178	136	63.5	5.784	0.724415	18	0.70978	8.69	41.9	0.1256	0.512229	18	−6.4	1.59	1.48
9705[b]	178	242	46.4	15.34	0.748624	20	0.70980	10.98	58.5	0.1138	0.512263	26	−5.4	1.35	1.41
Pitou amphibole-bearing alkali-feldspar granite															
PT03	178	163	87.6	5.38	0.722509	10	0.70888	16.2	101	0.0969	0.512306	6	−4.2	1.10	1.31
Dafengnao syenite															
DFN01	165	116	56.6	5.920	0.723725	11	0.70984	7.09	37.9	0.1131	0.512666	12	2.3	0.74	0.77
Tabei syenite															
GN22-2[c]	178	83	41.0	5.820	0.718298	16	0.70357	12.20	66.4	0.1111	0.512581	8	0.8	0.85	0.90
GN22-5[c]	178	83	52.3	4.600	0.714651	16	0.70301	25.10	126.0	0.1204	0.512580	9	0.6	0.93	0.92
GN22-6[c]	178	84	39.7	6.130	0.718323	16	0.70281	23.10	114.0	0.1225	0.512559	9	0.1	0.99	0.95
9701-3[b]	178	69.7	523	0.393	0.705172	14	0.70418	6.99	38.0	0.1114	0.512694	15	3.0	0.68	0.72
9702-1[b]	178	130	159	2.427	0.711916	15	0.70577	4.59	29.5	0.1158	0.512719	21	3.4	0.67	0.69
Huangbu syenite															
GN16-1[c]	178	126	48.1	7.570	0.723552	20	0.70439	9.00	43.5	0.1251	0.512618	6	1.2	0.92	0.86
GN16-3[c]	178	97.5	48.6	5.80	0.718889	35	0.70421	6.14	33.0	0.1125	0.512687	6	2.9	0.70	0.73
GN16-5[c]	178	80.2	46.6	4.980	0.717849	10	0.70525	5.09	24.8	0.1241	0.512734	7	3.5	0.71	0.68
GN16-7[c]	178	138	25.9	15.40	0.745800	15	0.70683	12.10	60.5	0.1209	0.512611	5	1.2	0.89	0.87
GN16-10[c]	178	137	47.6	8.32	0.723849	17	0.70279	8.63	39.9	0.1307	0.512643	6	1.6	0.93	0.83
GN16-11[c]	178	85.3	58.0	4.25	0.716893	13	0.70614	6.34	31.8	0.1205	0.512734	7	3.6	0.68	0.67
Chebu gabbro															
DLX3[d]	175	43.2	313	0.399	0.707630	13	0.70664	5.50	22.6	0.1471	0.512630	7	1.0	1.19	0.88
DLX10[d]	175	136	406	0.970	0.710612	14	0.70820	4.74	19.2	0.1493	0.512636	9	1.0	1.22	0.88
GN29-1[c]	175	65.1	267	0.705	0.708413	18	0.70666	4.60	18.6	0.1495	0.512613	10	0.6	1.28	0.92
GN29-4[c]	175	58.7	264	0.643	0.708105	17	0.70651	4.10	17.0	0.1458	0.512567	13	−0.2	1.31	0.98
GN29-5[c]	175	52.5	263	0.577	0.707955	14	0.70652	4.84	20.4	0.1434	0.512537	12	−0.8	1.33	1.03
99CB02[e]	175	58.8	307	0.554	0.707825	13	0.70645	5.09	22.2	0.1384	0.512569	13	0.0	0.97	1.18
Chenglong gabbro															
LN01	182	16.0	396	0.117	0.705059	10	0.70476	7.65	31.0	0.1493	0.512846	13	5.2	0.72	0.55

[a] Data from Zhang et al. (2006).
[b] Data from Chen et al. (2005).
[c] Data from Li et al. (2003).
[d] Data from Xie et al. (2005).
[e] Data from Hsieh et al. (2008).

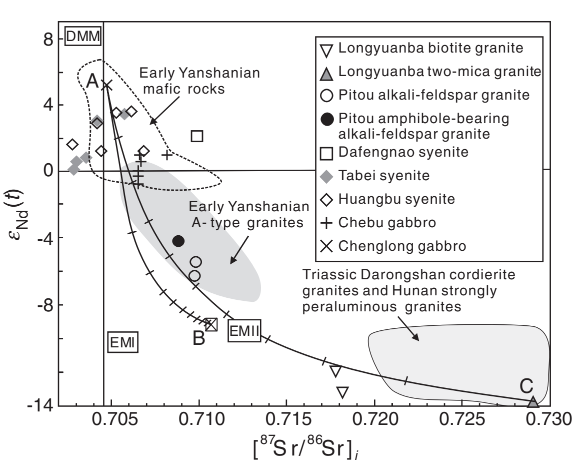

Fig. 10. $\varepsilon_{Nd}(t)$ vs. $[^{87}Sr/^{86}Sr]_i$ diagram for the GSGA rocks. Also shown are calculated binary mixing curves between possible end-members. Sample LN01 (Chenglong gabbro) represents the depleted mantle (A), lithosphere mantle (B) is represented by the Yangfang aegirite augite syenite in western Fujian (Wang et al., 2005a), YQ-57 (Longyuanba two-mica granite) represents crustal melt (C). Tick marks represent 10% intervals. Also illustrated for comparison are fields of Early Yanshanian mafic rocks (Xie et al., 2006; Chen et al., 2008b; Wang et al., 2003, 2005b, 2008b; Yu et al., 2010) and A-type granites from Southeast China (Li et al., 2003; 2007; Zhu et al., 2008) as well as Triassic Darongshan cordierite granites and Hunan S-type strongly peraluminous granites (Wang et al., 2007b; Hsieh et al., 2008). See text for discussion.

the extremely low bulk-rock $\varepsilon_{Nd}(t)$ and zircon $\varepsilon_{Hf}(t)$ and high $[^{87}Sr/^{86}Sr]_i$, which is similar to S-type Darongshan cordierite granites and strongly peraluminous granites in Hunan (Fig. 10). As per Chappell (1999), S-type granite was derived by partial melting of supracrustal rocks that have undergone some extent of weathering. Indeed, major components of crustal basement beneath the western Cathysia block are metamorphosed sedimentary rocks of late Neoproterozoic age, which are ideal source material for the S-type granite (Xu et al., 2007; Yu et al., 2007 and references therein). The metamorphic basement exposed near the study area includes Tanxi gneisses in the Nanxiong region and Xunwu gneisses in the Dingnan-Xunwu region. Zircon U–Pb age and Hf isotope studies show that their protoliths are dominated by Neoproterozoic meta-sedimentary rocks (Yu et al., 2007; Wang et al., 2008a). This is consistent with the inherited zircons of 596 Ma and 726 Ma in sample LYB03 of Longyuanba biotite granite. However, we cannot rule out the presence of older basement rocks as implied by the older Nd and Hf model ages (Table 4 and Electronic Data Table 2). In this context, it is important to emphasize that model ages are calculated from whole-rock Nd and zircon Hf isotopic compositions, whose values are, to a first order, the result of mixing of two more isotopically extreme lithologies involved or encountered during granitoid magmatism on land. If mantle input (heat and mass) is required for crustal melting and granitoid magmatism, as we argue below, then the mantle component would be more radiogenic (i.e., high positive $\varepsilon_{Nd}(t)$ and $\varepsilon_{Hf}(t)$ values) whereas the pre-existing crustal rocks would be less radiogenic (i.e., low and more negative $\varepsilon_{Nd}(t)$ and $\varepsilon_{Hf}(t)$ values). As a result, the crustal end-member would have even

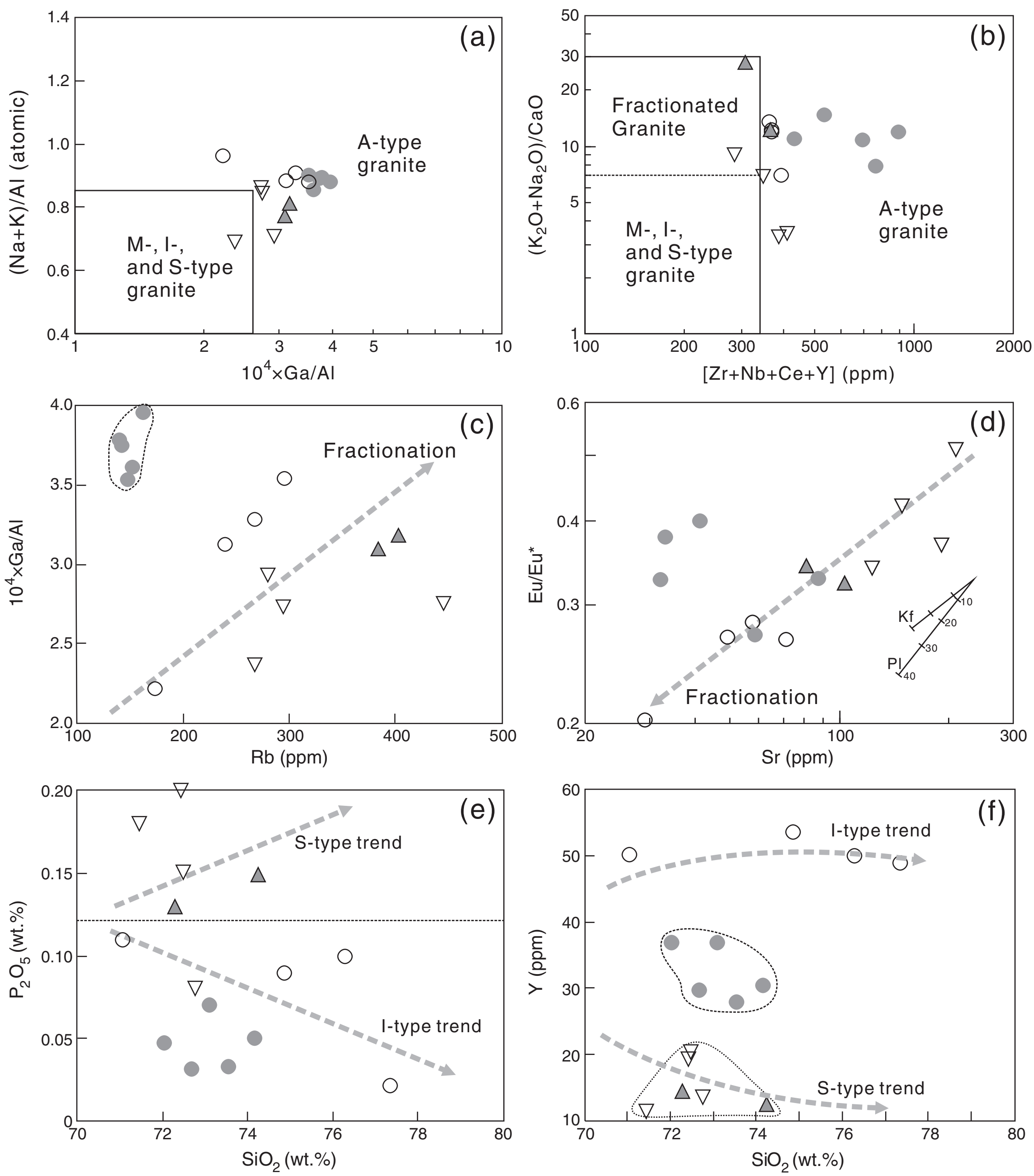

Fig. 11. Variation diagrams for the GSGA granites. (a) $10^4 \times$ Ga/Al vs. (Na + K)/Al (atomic) (after Whalen et al., 1987); (b) [Zr + Nb + Ce + Y] vs. ($Na_2O + K_2O$)/CaO (after Whalen et al., 1987); (c) $10^4 \times$ Ga/Al vs. Rb; (d) Eu/Eu* vs. Sr. Mineral vectors calculated according to partition coefficients compiled in Rollinson (1993); (e) P_2O_5 vs. SiO_2; (f) Y vs. SiO_2. The trend of I- and S-type granites follows Chappell (1999). Symbols are same as in Fig. 7.

more negative $\varepsilon_{Nd}(t)$ and $\varepsilon_{Hf}(t)$ values and the model ages should be even older than the calculated model ages. Likewise, the "mantle input member" would have even more positive $\varepsilon_{Nd}(t)$ and $\varepsilon_{Hf}(t)$ values, and the model ages should be even younger (Zhu et al., 2009). This analysis means that older basement rocks are likely present in the western Cathysia block even though they have not yet been directly observed and sampled.

As shown in Fig. 12, zircons from the Longyuanba biotite granite and two-mica granite all plot in the Neoproterozoic band of crustal evolution. So the Paleoproterozoic Hf model ages (1.7–2.1 Ga) of the samples should be an average age which resulted from mixing of continental materials of different ages. Likewise, their Paleoproterozoic (2.0–2.1 Ga) Nd model ages (Table 4) also reflect a similar mixing effect on bulk-rock $\varepsilon_{Nd}(t)$ values. So, it is not unreasonable to say that the basement rocks of the Cathysia block may be of Paleoproterozoic age (Chen and Jahn, 1998), but we emphasize that Archean basement rocks may indeed exist although they are yet to be recognized.

5.3. Relative contributions of crust and mantle to the petrogenesis of I- and A-type granite units

The I-type Pitou alkali-feldspar granites are ferroan, dominantly metaluminous, and have high HREEs, low $[^{87}Sr/^{86}Sr]_i$ and high bulk-rock $\varepsilon_{Nd}(t)$ and zircon $\varepsilon_{Hf}(t)$ relative to the S-type Longyuanba granites (Fig. 10 and 12). To explain the origin of I-type granites,

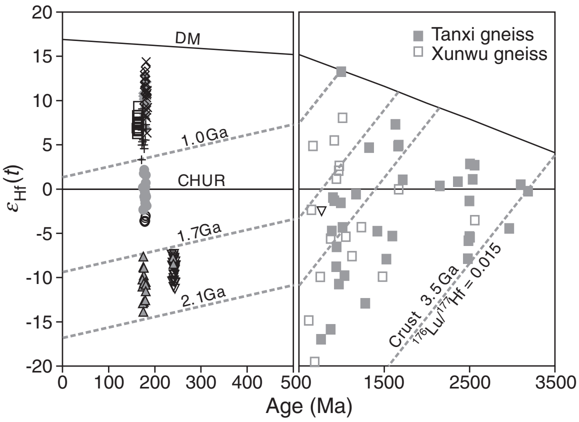

Fig. 12. Diagram of $\varepsilon_{Hf}(t)$ vs. U–Pb ages for zircons from the GSGA samples. The dashed lines of crustal extraction are calculated by using $^{176}Lu/^{177}Hf$ ratio of 0.015 for the average continental crust (Griffin et al., 2002). The data for the Tanxi gneisses and Xunwu gneisses are from Yu et al. (2007) and Wang et al. (2008a) respectively. Symbols are same as in Fig. 10.

Chappell and White (1974) suggested the model of partial melting of mafic to intermediate meta-igneous crustal rocks that had not experienced surface processes. Recently, the integrated *in situ* U–Pb, Hf, and O isotope study of zircons from granites has demonstrated that I-type granite may be formed by mixing of sedimentary materials and mantle-derived magmas instead of remelting ancient meta-igneous crustal rocks (Kemp et al., 2007; Zhu et al., 2009). The isotope data of Pitou alkali-feldspar granite favor this interpretation. As mentioned above, the western Cathysia block is dominated by crust of Neoproterozoic age with minor Archean to Mesoproterozoic components. The exposed metamorphic basements of Tanxi gneisses and Xunwu gneisses in the study area are Neoproterozoic meta-sedimentary rocks, and components of these rocks are mainly Grenville and Neoarchean clastic materials as well as some Mesoproterozoic and minor late Neoproterozoic and Mesoarchaean components. The Hf and Nd model ages of the Pitou alkali-feldspar granite (1.41–1.46 Ga and 1.41–1.48 Ga respectively, Table 4 and Electronic Data Table 2) are younger than those of the Longyuanba S-type granites which may represent an average age of ancient reworked crustal rocks. We thus suggest that the Pitou alkali-feldspar granite was likely produced by mixing of higher proportions of juvenile mantle-derived melts with the existing older crustal materials.

The Pitou amphibole-bearing alkali-feldspar granite is a ferroan granite (see Frost et al., 2001). The samples have high Ga/Al and Zr + Nb + Ce + Y and low Rb and Sr, and exhibit A-type-like granite characteristics (Whalen et al., 1987; Eby, 1992). They also have highest bulk-rock $\varepsilon_{Nd}(t)$ and zircon $\varepsilon_{Hf}(t)$ and lowest $[^{87}Sr/^{86}Sr]_i$ among the studied granitic units. Additionally, their Hf and Nd model ages are relatively young (1.08–1.37 Ga and 1.31 Ga respectively) (Table 4 and Electronic Data Table 2). Therefore, similar to the Pitou alkali-feldspar granite, a Neoproterozoic crustal source mixed with even higher proportions of mantle-derived melts best explains the petrogenesis of the Pitou amphibole-bearing alkali-feldspar granite. The mantle-derived melts required in their petrogenesis were most likely of asthenospheric origin as further manifested by zircon $\varepsilon_{Hf}(t) > 0$ afforded by some Pitou amphibole-bearing alkali-feldspar granite samples (Griffin et al., 2002; Zhu et al., 2009).

A simple mass balance calculation shows in $\varepsilon_{Nd}(t)$ vs. $[^{87}Sr/^{86}Sr]_i$ space a mixing curve (Fig. 10, curve AC) by using the Longyuanba two-mica granite as the crustal component and the Chenglong gabbro as representing the depleted mantle end-member. The results indicate that the I-type Pitou alkali-feldspar granite can be produced isotopically by mixing of ~45% of mantle-derived melt with crustal melts, while ~55% mantle-derived melt is required to explain the A-type Pitou amphibole-bearing alkali-feldspar granite. Thus, the mixing of different proportions of asthenospheric mantle-derived melt with crustal melts can account for granitoid melts parental to the coexisting I-type and A-type granites in South China.

5.4. Origin of the melts parental to gabbros and syenites and implications for the nature of mantle source

Like all gabbros, the Chenglong gabbros are likely cumulate rocks from mantle-derived basaltic magmas. This interpretation is consistent with the mantle isotopic signatures of the gabbroic samples, i.e., high bulk-rock $\varepsilon_{Nd}(t)$ (>0, 5.2) and high zircon $\varepsilon_{Hf}(t)$ (>0, 6.4 to 14.4). The straightforward explanation is that the basaltic magmas parental to the gabbros were derived from isotopically depleted asthenosphere. Furthermore, the incompatible element enriched signature (e.g., $[La/Sm]_{CN} > 1$) suggests that the parental basaltic magmas are consistent with low-degree melting of somewhat metasomatized source. Such low-degree partial melting of an asthenospheric source is tectonically compatible with a continental rift setting (e.g., Scarrow et al., 1998; Xu et al., 2005; Hollanda et al., 2006). In addition, the Chenglong gabbro has the most radiogenic Nd and Hf isotope compositions so far recorded for Mesozoic igneous rocks in South China (Xie et al., 2006; Wang et al., 2003, 2005b, 2008b; Li et al., 2009; Yu et al., 2010). Its $\varepsilon_{Hf}(t)$ and $\varepsilon_{Nd}(t)$ values are especially higher than those of Qinghu quartz monzonite from southeastern Guangxi ($\varepsilon_{Hf}(t) = 11.1$–$12.4$; $\varepsilon_{Nd}(t) = 4$–5; calculated for 160 Ma), which was suggested to represent the Mesozoic depleted mantle end-member of South China (Chen and Jahn, 1998; Li et al., 2009). Thus, the isotopic composition of Chenglong gabbros may be considered as the best estimates of the Mesozoic depleted mantle source beneath South China.

The $\varepsilon_{Nd}(t)$ values of Chebu gabbro show a large variation (from + 1 to − 0.8; Table 4), and the zircon $\varepsilon_{Hf}(t)$ values also vary (from 3.4 to 9.1; Electronic Data Table 2) with almost 6 ε_{Hf} units, which is consistent with open-system magma chamber processes at the crustal level. That is, the asthenospheric mantle-derived basaltic melt parental to the Chebu gabbro may be mixed with crustal components, producing the observed isotopic variability in the resultant gabbros.

Like the Chenglong and Chebu gabbros, all the syenite units (Huangbu, Tabei and Dafengnao) have depleted Sr–Nd–Hf isotopic features with positive $\varepsilon_{Nd}(t)$ and $\varepsilon_{Hf}(t)$ values, suggesting their parental melts are mantle-derived alkali-rich melts, most likely shoshonitic melts, genetically associated with partial melting K-rich metasomatized lithospheric mantle with hydrous phases such as amphibole or phlogopite (e.g., Turner et al., 1996; Scarrow et al., 1998; Conceição and Green, 2004; Conticelli et al., 2009). However, as suggested by Wang et al. (2005a) and Wang et al. (2008b), the subcontinental lithospheric mantle of South China is isotopically of EM-II type, and can be represented by the Yangfang aegirite augite syenite in western Fujian with an enriched isotopic signature (e.g., low bulk-rock $\varepsilon_{Nd}(t)$ of − 9.2 to − 10.6, high bulk-rock $[^{87}Sr/^{86}Sr]_i$ of 0.7107–0.7123 and low zircon $\varepsilon_{Hf}(t)$ values of − 7.5 to − 11.1) (also see Electronic Data Table 2; Figs. 6 and 10). We thus suggest that these syenites were likely produced by interaction of asthenosphere melts with metasomatized mantle lithosphere. In terms of Sr–Nd isotopes, the melts parental to the syenites might be derived from mixing of predominantly (~95%) depleted-asthenosphere-derived magmas with ~5% melts from enriched lithospheric mantle (Fig. 10; curve AB). The syenites resulted from significant fractional crystallization from these mantle-derived melts, giving rise to the highly evolved nature such as low MgO, Ni, Cr and high SiO_2. Additionally, the wide range of $\varepsilon_{Nd}(t)$ and $[^{87}Sr/^{86}Sr]_i$ in each syenite body and a rough negative correlation of $\varepsilon_{Nd}(t)$ with SiO_2 and LILE/HFSE ratios (e.g., K/Nb, Th/Nb and Th/La) (Fig. 13 shows Th/Nb variations) provide evidence for crustal contamination (e.g., Hollanda et al., 2006; Koszowska et al., 2007). Indeed, crustal assimilation is a natural

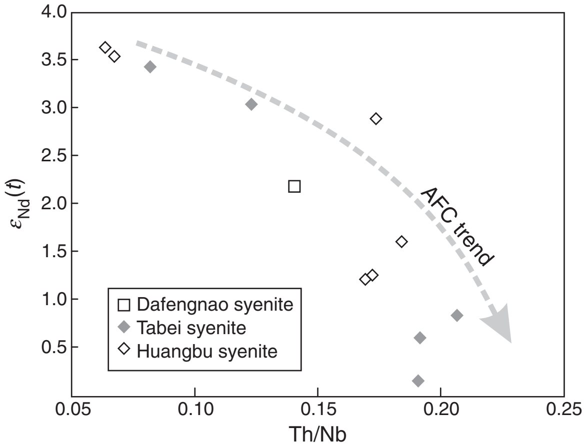

Fig. 13. Plot of $\varepsilon_{Nd}(t)$ value vs. Th/Nb ratio for the Dafengnao, Tabei and Huangbu syenites.

consequence of fractional crystallization dominated crustal level magma chamber processes (i.e., the AFC processes; DePaolo, 1981).

The lithospheric mantle is compositionally depleted in a melt component and thus physically buoyant. These physical and chemical properties facilitate the longevity of the lithosphere in isolation from the convective asthenosphere. On the other hand, because of low-degree melt metasomatism over its history, the mantle lithosphere in most cases has been refertilized and is thus enriched in volatiles, incompatible elements as well as isotopes (e.g., O'Reilly and Griffin, 1988; McKenzie, 1989; Rämö et al., 2003; Pilet et al., 2008). The isotopically enriched material mostly occurs as metasomatic veins or veinlets (e.g., Helvacı et al., 2009). The mantle lithosphere metasomatism beneath South China might be genetically associated with an ancient subduction event or may have undergone some similar metasomatic processes as taking place in the growing oceanic lithosphere (Niu, 2008), and may have remained untapped before the Early Yanshanian (Wang et al., 2008b). Because of volatile enrichments, metasomatic veins have a lower solidus than the host peridotite, and thus readily melt with thermal perturbation, possibly due to upwelling of the underlying asthenosphere under extensional tectonic setting. We propose that the intense magmatism in the interior of South China during the Early Yanshanian (Zhou et al., 2006) may have resulted from lithosphere extension probably as a response to the early stage of Pacific plate subduction (see below). This magmatism was sufficient to exhaust the enriched metasomatic component, leaving a refractory residue. The continued extension led to rising and melting of the fertile asthenosphere. This idea is supported by the late Cretaceous mafic rocks in the South China block hinterland (Jiangxi and Hunan Province), which are geochemically of asthenospheric origin with minimal lithospheric contribution (Wang et al., 2008b).

5.5. Implications for the Mesozoic tectonic evolution of South China

As noted above, the South China block has successively experienced two important tectonic episodes since the early Mesozoic, i.e., the Indosinian orogenic regime and the paleo-Pacific plate subduction regime, respectively. The concept of Indosinian Orogeny was originally defined on the basis of the geology in Vietnam, which is referred to as the synchronous oblique collision of Indochina with both Sibumasu and South China continental blocks in the early Triassic (Carter et al., 2001; Lepvrier et al., 2004). The kinematic and tectonothermal characteristics of Indosinian orogeny in the South China Block show a succession of events involving early middle Triassic thrusting-related transpression and development of a large-scale flower structure that developed in a regime of oblique regional convergence, and subsequent late Triassic transtension within the overthickened gravitationally unstable crustal segment (Wang et al., 2005c, 2007a). The Indosinian granites were emplaced in two episodes: the early Indosinian (243–228 Ma) and late Indosinian (220–206 Ma) (Wang et al., 2007b). The early Indosinian granites were thought to be generated by partial melting of thickened crust during the post-collisional episode under compressional conditions, induced by *in situ* radiogenic heating or increased geothermal gradient (Wang et al., 2007b). The late Indosinian granites were interpreted as resulting from dehydration melting of the crustal materials in a post-orogenic extensional setting (Wang et al., 2007b). Underplating of mantle-derived magmas were thought to have provided extra heat for the crustal melting as supported by the gabbroic xenoliths with mantle $\varepsilon_{Nd}(t)$ values and depleted mantle like zircon Hf isotopic compositions (with an age of ~220 Ma) at Daoxian in southern Hunan Province (Dai et al., 2008). In this study, the S-type Longyuanba biotite granite was emplaced at 240 Ma, and produced by reworking of the heterogeneous Neoproterozoic crust, which is consistent with those observed and predicted in post-collisional episode of Indosinian orogeny in South China (Wang et al., 2005c, 2007a,b).

Based on the occurrence of Jurassic E–W trending basalts and coexisting A-type granites and syenites in the interior of South China, Chen et al. (2002) and Chen et al. (2008b) proposed that the post-orogenic episode of Indosinian magmatism persisted to the Jurassic and these foregoing igneous rocks were comparable to the post-collision suites in extensional tectonic settings (Chen et al., 2002, 2008b). However, A-type granite and syenite could occur in a wide range of geodynamic settings, including post-collisional or anorogenic environments (e.g., Bonin, 2007). The Pitou A-type granite has low Y/Nb ratios (0.83–1.14), which is consistent with rift-related A_1-type granite (see Eby, 1992). Furthermore, the South China block was tectonically under compression in the Jurassic evidenced by the following geological observations: (1) very few late Middle Jurassic to Late Jurassic sedimentary sequences can be found in the region, which reflect uplift and erosion of the crust (Chen et al., 2007; Xing et al., 2008); (2) the Paleozoic and Early Mesozoic sequences underwent deformation marked by a series of NNE striking thrusts and folds of an Early Jurassic event (Zhang et al., 2009; Xu et al., 2009a); (3) the Early Cretaceous volcaniclastic strata unconformably overlie the Early Mesozoic sequences. For example, the Early Cretaceous Dongkeng volcanic basins in southern Jiangxi unconformably overlie the pre-Jurassic strata (Chen et al., 2007; Wang et al., 2008b), and the Early Cretaceous Nanyuan formation unconformably rests on the Early Jurassic Lishan formation or Late Triassic Wenbinshan formation in eastern Fujian (Xing et al., 2008). In addition, beside the existing E–W trending Jurassic magmatic belt, a Jurassic NE-trending A-type granite belt also exists in southern Hunan to central southern Guangxi with young T_{DM} and high $\varepsilon_{Nd}(t)$ relative to granites of the surrounding regions, implying significant mantle contributions to the petrogenesis of the A-type granite (Chen and Jahn, 1998; Zhu et al., 2008), which is inconsistent with east–west linear array expected from the post-collisional model (Chen et al., 2008b). Therefore, the Indosinian orogenesis must have ended in the Early Jurassic marked by a magmatically quiescent period of 205 to 180 Ma (Zhou et al., 2006; Yu et al., 2010), and another tectonic regime should be responsible for the generation of the Jurassic magmatism in South China.

Recently, Li and Li (2007) proposed a model of westward flat-slab subduction of the Pacific plate in the period of ~250–190 Ma to explain the regional tectonomagmatic evolution of South China in the Mesozoic. The authors interpreted the Jurassic magmatism as resulting from the break-off and foundering event of the subducting/subducted flat-slab in the Early Jurassic. However, this model is inconsistent with observations. Firstly, as argued by Chen et al. (2008b), there are no known Jurassic adakitic rocks in South China that would be expected as a result of broken slab melting (Omrani et al., 2008). Secondly, slab break-off should yield contemporaneous arc- and non-arc-like mafic magmas (Cvetković et al., 2004; Whalen et al., 2006), yet all the studied gabbros and syenites are of within-plate (anorogenic) origin without subduction-related magmatism. Thirdly, slab break-off should induce a linear heat pulse parallel to the subduction zone that would produce a relatively narrow, linear zone of magmatism (Davies and von Blanckenburg, 1995; Keskin et al., 2008), but all these are not observed. Fourthly, this model fails to explain the 500 km long E–W strike magmatic belt (Fig. 1a; Xie et al., 2006; Chen et al., 2008b). Finally, the Triassic tectonic elements define an E–W trend in South China (Zhang et al., 2009), indicating N–S compression as a result of northward collision of the Indochina block in the Triassic, which argues against the existence of westward subduction of the Pacific plate initiated at ~250 Ma.

Zhou et al. (2006) suggested a geodynamic model of two-stage subduction of the paleo-Pacific plate that provided a more appropriate tectonic framework for the observed Yanshanian magmatism in South China. In their model, the Jurassic igneous rocks correspond to an intraplate episode induced by initial subduction, while the successive Cretaceous magmatism corresponds to the active subduction stage. As discussed above, the granite–syenite–gabbro association of 180 Ma to 165 Ma in the interior of South China we present here documents the significance of asthenospheric mantle contribution to the petrogenesis of these rocks. We consider that these rocks may have well been produced as a consequence of the first intraplate stage of the two-stage model by Zhou et al. (2006), genetically associated with paleo-Pacific plate subduction.

It is now well established that the tectonic setting of South China in the Cretaceous is as an active continental margin (Andean-like) due to northwestward subduction of the paleo-Pacific plate, as manifested by the NE-trending volcanic-intrusive complexes distributed along the coastal area (Jahn, 1974; Gilder et al., 1996; Zhou et al., 2006; Li and Li. 2007; Chen et al., 2008a). The subduction may have initiated in the Early Jurassic (Jahn, 1974; Zhou and Li, 2000), and the convergence vector at that time was in the northwest direction determined from paleomagnetic data (Gilder et al., 1996; Ratschbacher et al., 2000). However, there was no continental magmatic arc developed during the Jurassic, as the subducting slab beneath South China may not have reached the ~100 km depth where the overlying hydrous metasomatized mantle is insufficiently hot to cause melting (Stern, 2002). The oblique convergence of the paleo-Pacific plate to South China block would have triggered reactivation of pre-existing faults or zones of lithosphere weakness in the interior in South China, whose geodynamic style is schematically shown in Fig. 14. Many Mesozoic left-lateral strike-slip faults have been mapped in south China (Xu et al., 1987). Of these, the most striking sinistral strike-slip faulting is the Shi-Hang zone (Gilder et al., 1996), which coincides with the Jurassic NE-trending belt

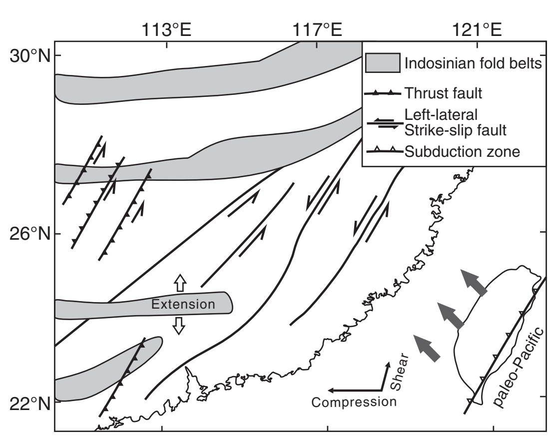

Fig. 14. Schematic representation for the tectonic configuration of the Early Yanshanian South China (modified after Gilder et al., 1996; Zhang et al., 2009).

of A-type granites, such as the Guposhan, Qitianling and Qianlishan (Fig. 1a; Jiang et al., 2006; Zhu et al., 2008). The reactivation of pre-existing structures would lead to the discrete and localized intraplate extension, which may allow asthenospheric mantle upwelling and decompression melting, which can in turn induce contemporaneous crustal melting for granitoid magmatism. The Jurassic igneous rocks are localized along major fracture zones and basaltic volcanoes are characterized by fissure eruptions, with which our interpretations agree. A similar model was proposed by Liégeois et al. (2005) for the genesis of the Cenozoic Hoggar volcanism in West Africa, which is a tectonic response to far-distance stress at plate margins during the Africa–Europe convergence. On the other hand, the far-field compressional stress can account for the uplift of the Jurassic crust and exposure of Jurassic and pre-Jurassic granitic plutons in the interior of South China as well as the existence of a regional unconformity between the Jurassic and Cretaceous throughout South China (Xing et al., 2008).

Mafic magmas produced by decompression melting of the asthenospheric mantle can infiltrate the lithosphere and react with metasomatized subcontinental lithospheric mantle for generating potassic magmas. The injection and ponding of these mantle-derived melts into crust can also cause crustal melting, giving rise to the coeval mantle- and crustal-derived melts and the hybrid magmatic complexes of the granite–syenite–gabbro association in time and space. The model is shown schematically in Fig. 15. In addition, the intra- or underplating of mantle-derived magmas provided sufficient heat to enhance the geothermal gradients, and the granitic magmas could undergo significant differentiation to form the related W-Sn mineralization (e.g., Hua et al., 2005; He et al., 2010). There were minor Jurassic magmatic activities along the South China coast, such as the Early Jurassic Maonong dacitic rocks and Longshan granite in Zhejiang (Chen et al., 2007). These are likely products of crustal anatectic melts under compressional regimes in the early stage of the paleo-Pacific plate subduction.

In conclusion, the tectonic transition from the Tethys orogenic regime to the paleo-Pacific regime was accomplished in the Early Jurassic, the Jurassic (Early Yanshanian) intraplate episode is interpreted to belong to the paleo-Pacific tectonic regime. The subsequent active subduction stage of paleo-Pacific tectonic regime is marked by the vast Cretaceous (Late Yanshanian) dacite and rhyolite (and minor andesite and basalt) volcanism distributed in the coastal area in South China (Chen et al., 2008a; Zhou et al., 2006).

6. Summary

(1) The granite–syenite–gabbro association in southern Jiangxi was emplaced in two major magmatic episodes, including the S-type biotite granite in the Indosinian, and granite–syenite–gabbro in the Early Yanshanian. In particular, the Early Yanshanian granites have different petrographic and chemical characteristics, showing a variety of S-, I- and A-type granites.
(2) The S-type granites were produced by melting of reworked Neoproterozoic crust in the western Cathysia; their Paleoproterozoic Hf and Nd model ages (1.7–2.1 Ga) represent a mixing effect of crustal materials of different ages.
(3) The I-type Pitou alkali-feldspar granite resulted from mixing of asthenosphere-derived melts with the induced Neoproterozoic crustal melt. The A-type Pitou amphibole-bearing alkali feldspar granite has a similar origin to that for the I-type Pitou alkali-feldspar granite, but has a much greater mantle contribution. This varying extent of crustal and mantle contributions in the petrogenesis of I- and A-type granites may be applicable to the petrogenesis of most Mesozoic I- and A-type granites in South China.
(4) The Chenglong gabbro is a body of magmatic cumulate from a basaltic melt formed by partial melting of upwelling asthenospheric mantle, and its isotopic composition may best

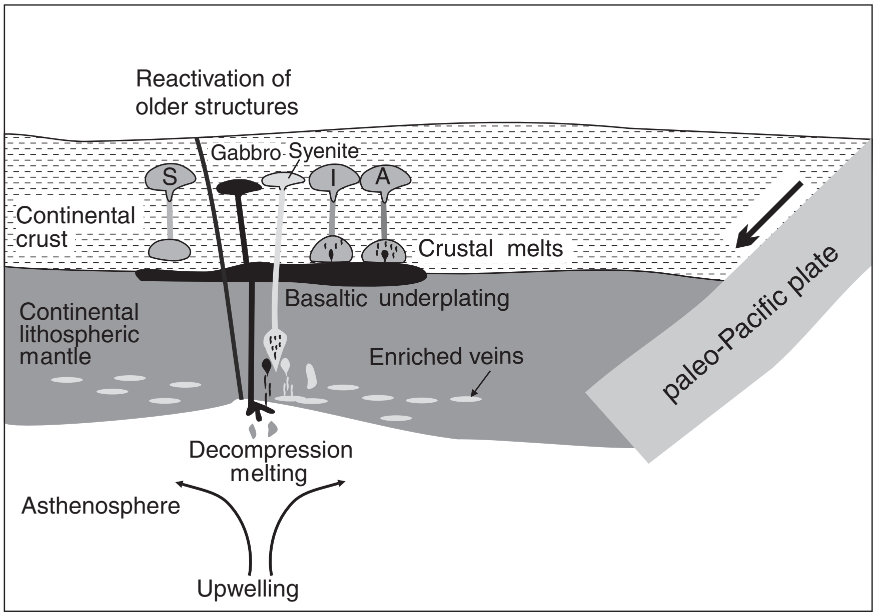

Fig. 15. Cartoon illustrating the magma genesis of the Jurassic granite–syenite–gabbro association (GSGA) in the inland South China. Reactivation of pre-existing structures (Fig. 14) can lead to lithospheric extension and spatially discrete and localized intraplate asthenospheric upwelling, decompression melting, and basaltic magmas parental to the gabbros. The enriched veins in the lithospheric mantle were preferentially melted under thermal perturbation with the melt mixed with the asthenosphere-derived magmas to produce the melts parental to the syenites. The intra- or underplating mantle-derived magmas caused partial melting of the crustal materials to produce S-type granites. In the same time, interactions between mantle- and crust-derived melts may give rise to I- and A-type granitic magmas. Relative to I-type granite, the A-type granite has much greater asthenospheric mantle contributions.

represent the depleted mantle source beneath South China in the Mesozoic. The syenites were the products of lithosphere–asthenosphere interactions as a result of mixing of asthenosphere-derived melt with enriched lithospheric mantle melt. Crustal assimilation associated with concurrent fractional crystallization is required to explain the large Nd–Sr–Hf isotopic variations in the Chebu gabbro and the more evolved syenites.

(5) Our studied granite–syenite–gabbro association in time and space emphasizes the primary role of asthenospheric mantle upwelling and magma generation in the Early Yanshanian granitoid magmatism in South China. The most likely tectonic model accounting for the genesis of these rocks involves a local intraplate environment in the interior of South China as a tectonic response to far-distance stress at plate margins during the early stage of the paleo-Pacific plate subduction. The Early Yanshanian event should belong to the paleo-Pacific tectonic regime.

Supplementary materials related to this article can be found online at doi:10.1016/j.lithos.2010.08.016

Acknowledgements

This work was supported by National Natural Science Foundation of China (Grant 40730313), Chinese Geological Survey Project (1212010632100) and a research grant (2008-I-02) from the State Key Laboratory for Mineral Deposits Research, Nanjing University. We are thankful to Tang, H. F. for his assistance with zircon Hf isotope analysis. G. Nelson Eby and two anonymous reviewers are thanked for their careful comments.

Appendix A

Mineral compositions were analyzed using a JEOL JXA-8100 microprobe in the State Key Laboratory for Mineral Deposits Research in Nanjing University (NJU). The operating conditions were 15 kV accelerating voltage, 20 nA beam current. For amphibole and pyroxene, the calibration standards used were hornblende (for Si, Ti, Al, Fe, Ca, Mg, Na and K), fayalite (for Mn) and Cr_2O_3 (for Cr).

Zircons were extracted using standard density and magnetic separation techniques. Selected zircon grains were hand-picked under a binocular microscope and were mounted in epoxy resin before polished to section the crystals in half for analysis. Zircon U–Pb dating of three samples (QN01, DN01 and LN01) was carried out using an Agilent 7500 ICP-MS coupled with a New Wave 213 nm laser sampler at GEMOC, Macquarie University, Australia. The instrumental settings and analytical details were described by Jackson et al. (2004). Back scattered electron (BSE) images of the selected zircons were collected using a Camebax SX 100 electron microprobe. The rest seven samples were analyzed using an Agilent 7500a ICP-MS equipped with a New Wave 213 nm laser sampler in the State Key Laboratory of Mineral Deposits Research, NJU. BSE images of analyzed zircons were obtained using a JEOL JXA-8100 microprobe. Detailed analytical procedures are given in Xu et al. (2009b). Common Pb contents were evaluated following Andersen (2002). The age calculations and plotting of concordia diagrams were done using Isoplot (ver 2.49) (Ludwig, 2001).

In situ Hf isotopic analyses on zircons from three samples (QN01, DN01 and LN01) were done using the combination of a New Wave 213 nm laser sampler and a Nu Plasma multi-collector ICP-MS at GEMOC, Macquarie University, Australia. During the analyses, a 5 Hz repetition rate with energy of 0.2 mJ/pulse was used, and spot size was 50 μm. The methodology and analyses of standard solutions and standard zircons are given in Griffin et al. (2000). The rest seven samples were analyzed in the Institute of Geochemistry, Chinese Academy of Sciences in Guiyang, China, using a Nu plasma MC-ICP-MS, equipped with a 213 nm laser sampler. The analysis was done with ablation pit of 60 μm in diameter, repetition rate of 10 Hz, ablation time of 60 s, and laser beam energy of 0.155 mJ/pulse. In order to evaluate the reliability of the data, zircon standard 91500 was analyzed during the course of this study and yielded a weighted mean $^{176}Hf/^{177}Hf$ ratio of 0.282309 ± 37 (2σ). The analytical details and interference correction method of ^{176}Yb on ^{176}Hf are given in Tang et al. (2008). The measured

$^{176}Lu/^{177}Hf$ ratios and the ^{176}Lu decay constant of 1.865×10^{-11} yr^{-1} (Scherer et al., 2001) were used to calculate initial $^{176}Hf/^{177}Hf$ ratios. The chondritic values of $^{176}Lu/^{177}Hf = 0.0332$ and $^{176}Hf/^{177}Hf = 0.282772$ (Blichert-Toft and Albarède, 1997) were used for calculating ε_{Hf} values. The depleted mantle Hf model ages (T_{DM}) were calculated using the measured $^{176}Lu/^{177}Hf$ ratios based on the assumption that the depleted mantle reservoir has a linear isotopic growth from $^{176}Hf/^{177}Hf = 0.279718$ at 4.55 Ga to 0.283250 at present, with $^{176}Lu/^{177}Hf = 0.0384$ (Griffin et al., 2000). We also present a two-stage model age (T_{DM2}) for each zircon, which assumes that its parental magma was produced from an average continental crust ($^{176}Lu/^{177}Hf = 0.015$) that was originally derived from the Depleted Mantle (Griffin et al., 2002).

Bulk-rock major element analysis was done using an ARL9800XP+ X-ray fluorescence spectrometer (XRF) in the Center of Modern Analysis, NJU. The analytical precision is generally better than 2% for all the elements. Trace element abundances were measured using Finnigan Element II ICP-MS in the State Key Laboratory of Mineral Deposit Research, NJU, which gives precisions better than 10% for most of the elements analyzed. The Sr and Nd isotopic compositions were measured using a Finnigan MAT262 thermal ionization mass spectrometer (TIMS) at the Institute of Geology and Geophysics, Chinese Academy of Sciences following the procedure of Zhang et al. (2002). Long-term laboratory measurements of the JNdi-1 Nd and NBS 987 Sr standards yield $^{143}Nd/^{144}Nd = 0.512105 \pm 12$ (2σ) and $^{87}Sr/^{86}Sr = 0.710272 \pm 10$ (2σ), respectively. The isotopic ratios were corrected for mass fractionation by normalizing to $^{146}Nd/^{144}Nd = 0.7219$ and $^{86}Sr/^{88}Sr = 0.1194$, respectively.

References

Andersen, T., 2002. Correction of common Pb in U–Pb analyses that do not report ^{204}Pb. Chem. Geol. 192, 59–79.
Blichert-Toft, J., Albarède, F., 1997. The Lu–Hf geochemistry of chondrites and the evolution of the mantle-crust system. Earth Planet. Sci. Lett. 148, 243–258.
Bonin, B., 2007. A-type granites and related rocks: evolution of a concept, problems and prospects. Lithos 97, 1–29.
Calanchi, N., Peccerillo, A., Tranne, C.A., Lucchini, F., Rossi, P.L., Kempton, P., Barbieri, M., Wu, T.W., 2002. Petrology and geochemistry of volcanic rocks from the island of Panarea: implications for mantle evolution beneath the Aeolian island arc (southern Tyrrhenian sea). J. Volcanol. Geoth. Res. 115, 367–395.
Carter, A., Roques, D., Bristow, C., 2001. Understanding Mesozoic accretion in southeast Asia: significance of Triassic thermotectonism (Indosinian orogen) in Vietnam. Geology 29, 211–214.
Chappell, B.W., 1999. Aluminium saturation in I- and S-type granites and the characterization of fractionated haplogranites. Lithos 46, 535–551.
Chappell, B.W., White, A.J.R., 1974. Two contrasting granite types. Pac. Geol. 8, 173–174.
Chen, J.F., Jahn, B.M., 1998. Crustal evolution of southeastern China: Nd and Sr isotopic evidence. Tectonophysics 284, 101–133.
Chen, P.R., Hua, R.M., Zhang, B.T., Lu, J.J., Fan, C.F., 2002. Early Yanshanian post-orogenic granitoids in the Nanling region — petrological constraints and geodynamic settings. Sci. China, Ser. D Earth Sci. 45, 755–768.
Chen, P.R., Zhou, X.M., Zhang, W.L., Li, H.M., Fan, C.F., Sun, T., Chen, W.F., Zhang, M., 2005. Petrogenesis and significance of early Yanshanian synite–granite complex in eastern Nanling Range. Sci. China, Ser. D Earth Sci. 48, 912–924.
Chen, R., Xing, G.F., Yang, Z.L., Zhou, Y.Z., Yu, M.G., Li, L.M., 2007. Early Jurassic zircon SHRIMP U–Pb age of the dacitic volcanic rocks in the southeastern Zhejiang Province, determined firstly and its geological Significances. Geol. Rev. 53, 32–35 (in Chinese with English abstract).
Chen, C.H., Lee, C.Y., Shinjo, R., 2008a. Was there Jurassic paleo-Pacific subduction in South China?: Constraints from $^{40}Ar/^{39}Ar$ dating, elemental and Sr–Nd–Pb isotopic geochemistry of the Mesozoic basalts. Lithos 106, 83–92.
Chen, C.H., Lee, C.Y., Lu, H.Y., Hsieh, P.S., 2008b. Generation of Late Cretaceous silicic rocks in SE China: age, major element and numerical simulation constraints. J. Asian Earth Sci. 31, 479–498.
Conceição, R.V., Green, D.H., 2004. Derivation of potassic (shoshonitic) magmas by decompression melting of phlogopite + pargasite lherzolite. Lithos 72, 209–229.
Conticelli, S., Guarnieri, L., Farinelli, A., Mattei, M., Avanzinelli, R., Bianchini, G., Boari, E., Tommasini, S., Tiepolo, M., Prelević, D., Venturelli, G., 2009. Trace elements and Sr–Nd–Pb isotopes of K-rich, shoshonitic, and calc-alkaline magmatism of the Western Mediterranean Region: genesis of ultrapotassic to calc-alkaline magmatic associations in a post-collisional geodynamic setting. Lithos 107, 68–92.
Cvetković, V., Prelević, D., Downes, H., Jovanović, M., Vaselli, O., Pécskay, Z., 2004. Origin and geodynamic significance of Tertiary postcollisional basaltic magmatism in Serbia (central Balkan Peninsula). Lithos 73, 161–186.
Dai, B.Z., Jiang, S.Y., Jiang, Y.H., Zhao, K.D., Liu, D.Y., 2008. Geochronology, geochemistry and Hf–Sr–Nd isotopic compositions of Huziyan mafic xenoliths, southern Hunan Province, South China: petrogenesis and implications for lower crust evolution. Lithos 102, 65–87.
Davies, J.H., von Blanckenburg, F., 1995. Slab breakoff: a model of lithosphere detachment and its test in the magmatism and deformation of collisional orogens. Earth Planet. Sci. Lett. 129, 85–102.
DePaolo, D.J., 1981. Trace element and isotopic effects of combined wallrock assimilation and fractional crystallization. Earth Planet. Sci. Lett. 53, 189–202.
Droop, G.T.R., 1987. A general equation for estimating Fe^{3+} concentrations in ferromagnesian silicates and oxides from microprobe analyses, using stoichiometric criteria. Mineralog. Mag. 51, 431–435.
Eby, G..N., 1992. Chemical subdivision of the A-type granitoids: petrogenetic and tectonic implications. Geology 20, 641–644.
Frost, B.R., Barnes, C.G., Collins, W.J., Arculus, R.J., Ellis, D.J., Frost, C.D., 2001. A geochemical classification for granitic rocks. J. Petrol. 42, 2033–2048.
Gilder, S.A., Gill, J., Coe, R.S., Zhao, X.X., Liu, Z.W., Wang, G.X., Yuan, K.R., Liu, W.L., Kuang, G..D., Wu, H.R., 1996. Isotopic and paleomagnetic constraints on the Mesozoic tectonic evolution of south China. J. Geophys. Res. 101, 16137–16154.
Griffin, W.L., Pearson, N.J., Belousova, E., Jackson, S.E., O'Reilly, S.Y., van Achterberg, E., Shee, S.R., 2000. The Hf-isotope composition of cratonic mantle: LAM-MC–ICPMS analysis of zircon megacrysts in kimberlites. Geochim. Cosmochim. Acta 64, 133–147.
Griffin, W.L., Wang, X., Jackson, S.E., Pearson, N.J., O'Reilly, S.Y., 2002. Zircon geochemistry and magma mixing, SE China: in-situ analysis of Hf isotopes, Tonglu and Pingtan igneous complexes. Lithos 61, 237–269.
He, Z.Y., Xu, X.S., Chen, R., Xing, G.F., 2007. Genesis of Middle Jurassic syenite–gabbro in southern Jiangxi province and their geological significance. Acta Petrol. Sin. 23, 1457–1469 (in Chinese with English abstract).
He, Z.Y., Xu, X.S., Yu, Y., Zou, H.B., 2009. Origin of the Late Cretaceous syenite from Yandangshan, SE China, constrained by zircon U–Pb and Hf isotopes and geochemical data. Int. Geol. Rev. 51, 556–582.
He, Z.Y., Xu, X.S., Zou, H.B., Wang, X.D., Yu, Y., 2010. Geochronology, petrogenesis and metallogeny of Piaotang granites in the tungsten deposit region of South China. Geochemical Journal 44, 299–313.
Helvacı, C., Ersoy, E.Y., Sözbilir, H., Erkül, F., Sümer, Ö., Uzel, B., 2009. Geochemistry and $^{40}Ar/^{39}Ar$ geochronology of Miocene volcanic rocks from the Karaburun Peninsula: implications for amphibole-bearing lithospheric mantle source, Western Anatolia. J. Volcanol. Geoth. Res. 185, 181–202.
Hollanda, M.H.B.M., Pimentel, M.M., Oliveira, D.C., de Sá, E.F.J., 2006. Lithosphere–asthenosphere interaction and the origin of Cretaceous tholeiitic magmatism in Northeastern Brazil: Sr–Nd–Pb isotopic evidence. Lithos 86, 34–49.
Hsieh, P.S., Chen, C.H., Yang, H.J., Lee, C.Y., 2008. Petrogenesis of the Nanling Mountains granites from South China: constraints from systematic apatite geochemistry and whole-rock geochemical and Sr–Nd isotope compositions. J. Asian Earth Sci. 33, 428–451.
Hua, R.M., Chen, P.R., Zhang, W.L., Yao, J.M., Lin, J.F., Zhang, Z.S., Gu, S.Y., 2005. Metallogeneses and their geodynamic settings related to Mesozoic granitoids in the Nanling Range. Geol. J. Chin. Univ. 11, 291–304 (in Chinese with English abstract).
Irvine, T.N., 1987. Glossary of terms for layered intrusions. In: Parsons, I. (Ed.), Origins of Igneous Layering. Reidel, Dortrecht, pp. 641–647.
Jackson, S.E., Pearson, N.J., Belousova, E.A., 2004. The application of laser ablation–inductively coupled plasma–massspectrometry to in situ U–Pb zircon geochronology. Chem. Geol. 211, 47–69.
Jahn, B.M., 1974. Mesozoic thermal events in southeast China. Nature 248, 480–483.
Jahn, B.M., Zhou, X.H., Li, J.L., 1990. Formation and tectonic evolution of southeastern China and Taiwan: isotopic and geological constraints. Tectonophysics 183, 145–160.
Jiang, Y.H., Jiang, S.Y., Zhao, K.D., Ling, H.F., 2006. Petrogenesis of Late Jurassic Qianlishan granites and mafic dykes, Southeast China: implications for a back-arc extension setting. Geol. Mag. 143, 457–474.
Kemp, A.I.S., Hawkesworth, C.J., Foster, G..L., Paterson, B.A., Woodhead, J.D., Hergt, J.M., Gray, C.M., Whitehouse, M.J., 2007. Magmatic and crustal differentiation history of granitic rocks from hafnium and oxygen isotopes in zircon. Science 315, 980–983.
Keskin, M., Genç, Ş.C., Tüysüz, O., 2008. Petrology and geochemistry of post-collisional Middle Eocene volcanic units in North-Central Turkey: evidence for magma generation by slab breakoff following the closure of the Northern Neotethys Ocean. Lithos 104, 267–305.
King, P.L., Chappell, B.W., Allen, C.M., White, A.J.R., 2001. Are A-type granites the high-temperature felsic granites? Evidence from fractionated granites of the Wangrah Suite. Aust. J. Earth Sci. 48, 501–514.
Koszowska, E., Wolska, A., Zuchiewicz, W., Cuong, N.Q., Pécskay, Z., 2007. Crustal contamination of Late Neogene basalts in the Dien Bien Phu Basin, NW Vietnam: some insights from petrological and geochronological studies. J. Asian Earth Sci. 29, 1–17.
Leake, B.E., Woolley, A.R., Arps, C.E.S., Birch, W.D., Gilbert, M.C., Grice, J.D., Hawthorne, C., Kato, A., Kisch, H.J., Krivovichev, V.G., Linthout, K., Laird, J., Mandarino, J.A., Maresch, W.V., Nickel, E.H., Rock, N.M.S., Schumacher, J.C., Smith, D.C., Stephenson, N.C.N., Ungaretti, L., Whittaker, E.J.W., Youzhi, G., 1997. Nomenclature of amphiboles: report of the Subcommittee on Amphiboles of the International Mineralogical Association, Commission on New Minerals and Mineralnames. Am. Mineralog. 82, 1019–1037.
Lepvrier, C., Maluski, H., Tich, Vu., Van Leyerloup, A., Phan Truong, T., Nguyen Van, V., 2004. The Early Triassic Indosinian orogeny in Vietnam (Truong Son Belt and Kontum Massif); implications for the geodynamic evolution of Indochina. Tectonophysics 393, 87–118.

Li, Z.X., Li, X.H., 2007. Formation of the 1300 km-wide intra-continental orogen and post-orogenic magmatic province in Mesozoic South China: a flat-slab subduction model. Geology 35, 179–182.
Li, X.H., Chen, Z.G., Liu, D.Y., Li, W.X., 2003. Jurassic gabbro–granite–syenite suites from southern Jiangxi Province, SE China: age, origin and tectonic significance. Int. Geol. Rev. 45, 898–921.
Li, X.H., Li, Z.X., Li, W.X., Liu, Y., Yuan, C., Wei, G.J., Qi, C.S., 2007. U–Pb zircon, geochemical and Sr–Nd–Hf isotopic constraints on age and origin of Jurassic I- and A-type granites from central Guangdong, SE China: a major igneous event in response to foundering of a subducted flat-slab? Lithos 96, 186–204.
Li, X.H., Li, W.X., Wang, X.C., Li, Q.L., Liu, Y., Tang, G.Q., 2009. Role of mantle-derived magma in genesis of early Yanshanian granites in the Nanling Range, South China: in situ zircon Hf-O isotopic constraints. Sci. China, Ser. D Earth Sci. 52, 1262–1278.
Liégeois, J.P., Benhallou, A., Azzouni-Sekkal, A., Yahiaoui, R., Bonin, B., 2005. The Hoggar swell and volcanism, Tuareg shield, Central Sahara: intraplate reactivation of Precambrian structures as a result of Alpine convergence. In: Foulger, G.R., Natland, J.H., Presnall, D.C., Anderson, D.L. (Eds.), Plates, Plumes and Paradigms. Geological Society of America Special Paper 388, pp. 379–400.
Ludwig, K.R., 2001. Users Manual for Isoplot/Ex (rev. 2.49): a geochronological toolkit for microsoft excel. Berkeley Geochronology Center, Special Publication No. 1a, 55.
McKenzie, D.P., 1989. Some remarks on the movement of small melt fractions in the mantle. Earth Planet. Sci. Lett. 95, 53–72.
Meng, Q.R., Zhang, G.W., 2000. Geologic framework and tectonic evolution of the Qinling orogen, Central China. Tectonophysics 323, 183–196.
Middlemost, E.A.K., 1994. Naming materials in the magma/igneous rock system. Earth Sci. Rev. 37, 215–224.
Mo, X.X., Niu, Y.L., Dong, G.C., Zhao, Z.D., Hou, Z.Q., Zhou, S., Ke, S., 2008. Contribution of syncollisional felsic magmatism to continental crust growth: a case study of the Paleogene Linzizong Volcanic Succession in southern Tibet. Chem. Geol. 250, 49–67.
Morimoto, N., Fabries, J., Ferguson, A.K., Ginzbury, I.V., Ross, M., Serifert, F.A., Zussman, J., Aoki, K., Gottardi, G., 1988. Nomenclature of pyroxenes. Mineralog. Mag. 52, 535–550.
Niu, Y.L., 2008. The origin of alkaline lavas. Science 320, 883–884.
Niu, Y.L., O'Hara, M.J., 2009. MORB mantle hosts the missing Eu (Sr, Nb, Ta and Ti) in the continental crust: new perspectives on crustal growth, crust–mantle differentiation and chemical structure of oceanic upper mantle. Lithos 112, 1–17.
Niu, Y.L., Gilmore, T., Mackie, S., Greig, A., Bach, W., 2002. Mineral chemistry, whole-rock compositions and petrogenesis of ODP Leg 176 gabbros: data and discussion. In: Natland, J.H., Dick, H.J.B., Miller, D.J., Von Herzen, R.P. (Eds.), Proceedings of the Ocean Drilling Program, Scientific Results 176, p. 60.
Omrani, J., Agard, P., Whitechurch, H., Benoit, M., Prouteau, G., Jolivet, L., 2008. Arc-magmatism and subduction history beneath the Zagros Mountains, Iran: a new report of adakites and geodynamic consequences. Lithos 106, 380–398.
O'Reilly, S.Y., Griffin, W.L., 1988. Mantle metasomatism beneath western Victoria, Australia: I. Metasomatic processes in Cr-diopside lherzolites. Geochim. Cosmochim. Acta 52, 433–447.
Pearce, J.A., Harris, N.W., Tindle, A.G., 1984. Trace element discrimination diagrams for the tectonic interpretation of granitic rocks. J. Petrol. 25, 956–983.
Peccerillo, R., Taylor, S.R., 1976. Geochemistry of Eocene calcalkaline volcanic rocks from the Kastamonu area, northern Turkey. Contrib. Mineralog. Petrol. 58, 63–81.
Pilet, S., Baker, M.B., Stolper, E.M., 2008. Metasomatized lithosphere and the origin of alkaline lavas. Science 320, 916–919.
Pirajno, F., Ernst, R.E., Borisenko, A.S., Fedoseev, G., Naumov, E.A., 2009. Intraplate magmatism in Central Asia and China and associated metallogeny. Ore Geol. Rev. 35, 114–136.
Rämö, O.T., McLemore, V.T., Hamilton, M.A., Kosunen, P.J., Heizler, M., Haapala, I., 2003. Intermittent 1630–1220 Ma magmatism in central Mazatal province: new geochronologic piercing points and some tectonic implications. Geology 31, 335–338.
Ratschbacher, L., Hacker, B.R., Webb, L.E., McWilliams, M., Ireland, T., Dong, S., Calvert, A., Chateigner, D., 2000. Exhumation of the ultrahigh-pressure continental crust in east central China: Cretaceous and Cenozoic unroofing and the Tan-Lu fault. J. Geophys. Res. 105, 13303–13338.
Rollinson, H.R., 1993. Using Geochemical Data: Evaluation, Presentation. Interpretation, Longman, John Wylie and Sons.
Scarrow, J.H., Leat, P.T., Wareham, C.D., Millar, L.L., 1998. Geochemistry of mafic dykes in the Antarctic Peninsula continental-margin batholith: a record of arc evolution. Contrib. Mineralog. Petrol. 131, 289–305.
Scherer, E., Munker, C., Mezger, K., 2001. Calibration of the Lutetium–Hafnium clock. Science 293, 683–687.
Stern, R.J., 2002. Subduction zones. Rev. Geophys. 40 (4), 1012.
Sun, S.S., McDonough, W.F., 1989. Chemical and isotopic systematics of oceanic basalts: implications for mantle composition and processes. In: Saunders, A.D., Norry, M.J. (Eds.), Magmatism in the Ocean Basins. Special Publications 42, Geological Society, London, pp. 313–345.
Tang, H.F., Zhao, Z.Q., Huang, R.S., Han, Y.J., Su, Y.P., 2008. Primary Hf isotopic study on zircons from the A-type granites in eastern Junggar of Xinjiang. Northwest China. Acta Mineral. Sin. 28, 335–342 (in Chinese with English abstract).
Taylor, S.R., McLennan, S.M., 1985. The continental Crust: Its Composition and Evolution. Blackwell, London.
Turner, S., Arnaud, N., Liu, J., Rogers, N., Hawkesworth, C., Harris, N., Kelley, S., van Calsteren, P., Deng, W., 1996. Postcollision, shoshonitic volcanism on the Tibetan, plateau: implications for convective thinning of the lithosphere and source of ocean island basalts. J. Petrol. 37, 45–71.
Wang, Y.J., Fan, W.M., Guo, F., Peng, T.P., Li, C.W., 2003. Geochemistry of Mesozoic mafic rocks adjacent to the Chenzhou-Linwu fault, South China: implication for the lithosphere boundary between the Yangtz and Cathaysia blocks. Int. Geol. Rev. 45, 263–286.
Wang, Q., Li, J.W., Jian, P., Zhao, Z.H., Xiong, X.L., Bao, Z.W., Xu, J.F., Li, C.F., Ma, J.L., 2005a. Alkaline syenites in eastern Cathaysia (South China): link to Permian–Triassic transtension. Earth Planet. Sci. Lett. 230, 339–354.
Wang, Y.J., Fan, W.M., Peng, T.P., Guo, F., 2005b. Elemental and Sr–Nd isotopic systematics of the early Mesozoic volcanic sequence in southern Jiangxi Province, South China: petrogenesis and tectonic implications. Int. J. Earth Sci. 94 (1), 53–65.
Wang, Y.J., Zhang, Y.H., Fan, W.M., Peng, T.P., 2005c. Structural signatures and $^{40}Ar/^{39}Ar$ geochronology of the Indosinian Xuefengshan tectonic belt, South China Block. J. Struct. Geol. 27 (6), 985–998.
Wang, Y.J., Fan, W.M., Cawood, P.A., Ji, S.C., Peng, T.P., Chen, X.Y., 2007a. Indosinian high-strain deformation for the Yunkaidashan tectonic belt, south China. Kinematics and $^{40}Ar/^{39}Ar$ geochronological constraints. Tectonics 26, TC6008.
Wang, Y.J., Fan, W.M., Sun, M., Liang, X.Q., Zhang, Y.H., Peng, T.P., 2007b. Geochronological, geochemical and geothermal constraints on petrogenesis of the Indosinian peraluminous granites in the South China Block: a case study in the Hunan Province. Lithos 96, 475–502.
Wang, L.J., Yu, J.H., O'Reilly, S.Y., Griffin, W.L., Sun, T., Wei, Z.Y., Jiang, S.Y., Shu, L.S., 2008a. Grenvillian orogeny in the Southern Cathaysia Block: constraints from U–Pb ages and Lu–Hf isotopes in zircon from metamorphic basement. Chin. Sci. Bull. 53, 3037–3050.
Wang, Y.J., Fan, W.M., Cawood, P.A., Li, S.Z., 2008b. Sr–Nd–Pb isotopic constraints on multiple mantle domains for Mesozoic mafic rocks beneath the South China Block hinterland. Lithos 106, 297–308.
Whalen, J.B., Currie, K.L., Chappell, B.W., 1987. A-type granites: geochemical characteristics, discrimination and petrogenesis. Contrib. Mineralog. Petrol. 95, 407–419.
Whalen, J.B., McNicoll, V.J., van Staal, C.R., Lissenberg, C.J., Longstaffe, F.J., Jenner, G.A., van Breeman, O., 2006. Spatial, temporal and geochemical characteristics of Silurian collision-zone magmatism, Newfoundland Appalachians: an example of a rapidly evolving magmatic system related to slab break-off. Lithos 89, 377–404.
Wilkinson, J.F.G., Le Maitre, R.W., 1987. Upper mantle amphiboles and micas and TiO_2, K_2O, and P_2O_5 abundances and 100 $Mg/(Mg+Fe^{2+})$ ratios of common basalts and andesites: implications for modal mantle metasomatism and undepleted mantle compositions. J. Petrol. 28, 37–73.
Xie, G.Q., Mao, J.W., Hu, R.Z., Li, R.L., Jiang, G.H., Cao, J.J., Zhao, J.H., 2005. Jurassic intraplate basaltic magmatism in Southeast China: evidence from geological and geochemical characteristics of the Chebu gabbroite in southern Jiangxi Province. Acta Geol. Sin.-English Edition 79, 662–672.
Xie, X., Xu, X.S., Zou, H.B., Jiang, S.Y., Zhang, M., Qiu, J.S., 2006. Early J_2 basalts in SE China: incipience of large-scale late Mesozoic magmatism. Sci. China, Ser. D Earth Sci. 49, 796–815.
Xing, G.F., Lu, Q.D., Chen, R., Zhang, Z.Y., Nie, T.C., Li, L.M., Huan, G.J., Lin, M., 2008. Study on the ending time of Late Mesozoic tectonic regime transition in South China: comparing to the Yanshan area in North China. Acta Geol. Sin. 82, 451–463 (in Chinese with English abstract).
Xu, J.W., Zhu, G., Tong, W.X., Cui, K.R., Liu, Q., 1987. Formation and evolution of the Tancheng–Lujiang wrench fault system: a major shear system to the northwest of the Pacific Ocean. Tectonophysics 134, 273–310.
Xu, Y.G., Ma, J.L., Frey, F.A., Feigenson, M.D., Liu, J.F., 2005. Role of lithosphere–asthenosphere interaction in the genesis of Quaternary alkali and tholeiitic basalts from Datong, western North China Craton. Chem. Geol. 224, 247–271.
Xu, X.S., O'Reilly, S.Y., Griffin, W.L., Wang, X.L., Pearson, N.J., He, Z.Y., 2007. The Crust of Cathaysia: age, assembly and reworking of two Terranes. Precambrian Res. 158, 51–78.
Xu, X.B., Zhang, Y.Q., Jia, D., Shu, L.S., Wang, R.R., 2009a. Early Mesozoic geotectonic processes in South China. Geol. China 36, 573–591 (in Chinese with English abstract).
Xu, X.S., Griffin, W.L., Ma, X., O'Reilly, S.Y., He, Z.Y., Zhang, C.L., 2009b. The Taihua group on the southern margin of the North China craton: further insights from U–Pb ages and Hf isotope compositions of zircons. Mineral. Petrol. 97, 43–59.
Yu, J.H., O'Reilly, S.Y., Wang, L.J., Griffin, W.L., Jiang, S.Y., Wang, R.C., Xu, X.S., 2007. Finding of ancient materials in Cathaysia and implication for the formation of Precambrian crust. Chin. Sci. Bull. 52, 13–22.
Yu, X.Q., Wu, G.G., Zhao, X.X., Gao, J.F., Di, Y.J., Zheng, Y., Dai, Y.P., Li, C.L., Qiu, J.T., 2010. The Early Jurassic tectono-magmatic events in southern Jiangxi and northern Guangdong provinces, SE China: constraints from the SHRIMP zircon U–Pb dating. J. Asian Earth Sci. 39, 408–422.
Zhang, Z.J., Wang, Y.H., 2007. Crustal structure and contact relationship revealed from deep seismic sounding data in South China. Phys. Earth Planet. Inter. 165, 114–126.
Zhang, H.F., Sun, M., Zhou, X.H., 2002. Mesozoic lithosphere destruction beneath the North China Craton: evidence from major-, trace-element and Sr–Nd–Pb isotope studies of Fangcheng basalts. Contrib. Mineralog. Petrol. 144, 241–253.
Zhang, M., Chen, P.R., Huang, G.L., Ling, H.F., 2006. The research on the geochemical characteristics of Longyuanba composite pluton in Nanling region. Uranium Geol. 22, 336–344 (in Chinese with English abstract).
Zhang, Y.Q., Xu, X.B., Jia, D., Shu, L.S., 2009. Deformation record of the change from Indosinian collision-related tectonic system to Yanshanian subduction-related tectonic system in South China during the Early Mesozoic. Earth Sci. Front. 16, 234–247 (in Chinese with English abstract).
Zheng, Y.F., Zhang, S.B., Zhao, Z.F., Wu, Y.B., Li, X.H., Li, Z.X., Wu, F.Y., 2007. Contrasting zircon Hf and O isotopes in the two episodes of Neoproterozoic granitoids in South China: implications for growth and reworking of continental crust. Lithos 96, 127–150.
Zhou, X.M., Li, W.X., 2000. Origin of late Mesozoic igneous rocks in Southeast China: implications for lithosphere subduction and underplating of mafic magmas. Tectonophysics 326, 269–287.

Zhou, J.C., Jiang, S.Y., Wang, X.L., Yang, J.H., Zhang, M.Q., 2005. Re–Os isochron age of Fankeng basalts from Fujian of SE China and its geological significance. Geochem. J. 39 (6), 497–502.
Zhou, X.M., Sun, T., Shen, W.Z., Shu, L.S., Niu, Y.L., 2006. Petrogenesis of Mesozoic granitoids and volcanic rocks in South China: a response to tectonic evolution. Episodes 29, 26–33.
Zhu, J.C., Chen, J., Wang, R.C., Lu, J.J., Xie, L., 2008. Early Yanshanian NE treading Sn/W-bearing A-type granites in the western-middle part of the Nanling Mts Region. Geol. J. China Univ. 14, 474–484 (in Chinese with English abstract).
Zhu, D.C., Mo, X.X., Niu, Y.L., Zhao, Z.D., Wang, L.Q., Liu, Y.S., Wu, F.Y., 2009. Geochemical investigation of Early Cretaceous igneous rocks along an east-west traverse throughout the central Lhasa Terrane, Tibet. Chem. Geol. 268, 298–312.